

Hysteresis, Impedance, and Transients Effects in Halide Perovskite Solar Cells and Memory Devices Analysis by Neuron-Style Models

Juan Bisquert

Halide perovskites are at the forefront of active research in many applications, such as high performance solar cells, photodetectors, and synapses and neurons for neuromorphic computation. As a result of ion transport and ionic-electronic interactions, current and recombination are influenced by delay and memory effects that cause hysteresis of current–voltage curves and long switching times. A methodology to formulate device models is shown, in which the conduction and recombination electronic variables are influenced by internal state variables. The models are inspired in biological frameworks of the Hodgkin–Huxley class of models. Here, the theoretical precedents, the main physical components of the models, and their application to describe dynamical measurements in halide perovskite devices are summarized. The application of several measurement methods is analyzed, as the current–voltage curves at different scan rates, the impedance spectroscopy response, and the time transients. The transition from normal (capacitive) to inverted (inductive) hysteresis, and the convergence of current–voltage curves to a stable value, are described. It is proposed that neuron-style models capture dynamical complexity with a favorable economy of parameters, toward the identification of the dominant global dynamic processes across a wide voltage span that determines the practical response of different types of devices.

This fascination stems from their remarkable ability to achieve power-conversion efficiencies surpassing 25%, a milestone that has propelled them to the forefront of cutting-edge solar cell technologies.^[1,2] The unique appeal of halide perovskites lies not only in their impressive performance but also in the simplicity of their solution-based processing methods. This combination of efficiency and ease of fabrication has launched intense exploration into the potential of halide perovskite solar cells, positioning them as a promising frontier in the pursuit of sustainable and high-performance photovoltaic systems. In this dynamic landscape, researchers are unraveling the intricate properties of halide perovskites, aiming to harness their full potential and pave the way for a new era in solar energy harvesting.


Early on in the research of halide perovskite solar cells (PSC) it emerged that they display important additional phenomena that are not included in the usual catalogue of semiconductor photovoltaic models.^[3] Certain dynamic

1. Introduction

Over the last decade, the realm of photovoltaics has witnessed a surge in research interest centered around halide perovskites.

J. Bisquert
Instituto de Tecnología Química
Universitat Politècnica de València-Consejo Superior de Investigaciones Científicas (UPV-CSIC)
Avd. dels Tarongers s/n, València 46022, Spain
E-mail: bisquert@uji.es

J. Bisquert
Institute of Advanced Materials (INAM)
Universitat Jaume I
Castelló 12006, Spain

 The ORCID identification number(s) for the author(s) of this article can be found under <https://doi.org/10.1002/aenm.202400442>

© 2024 The Authors. Advanced Energy Materials published by Wiley-VCH GmbH. This is an open access article under the terms of the [Creative Commons Attribution](#) License, which permits use, distribution and reproduction in any medium, provided the original work is properly cited.

DOI: 10.1002/aenm.202400442

effects in timescales that are much longer than electronic kinetics are present, such as a large low-frequency capacitance,^[4,5] slow photoconductivity and photovoltage response,^[6–10] and the famous dynamic hysteresis of current–voltage curves.^[11–20] Most of such effects can be due to the fact that the halide perovskites contain mobile ions.^[21] These ions undergo a slow reorganization under external light or voltage stimuli applied to the device, causing both ionic motion, and also coupled ionic-electronic effects.^[22–25] Using a variety of experimental characterization techniques, such as impedance spectroscopy and phototransients, a number of peculiar phenomena such as negative capacitance inductive effects,^[3,26–30] and anomalous time transients,^[31–35] have been broadly reported and discussed.

Early reports indicated the measurement fallacies that happen by hysteresis effects, e.g. larger efficiency by prepolarizing procedures.^[36] It has become apparent the need to control these phenomena, not only for the reliable measurement of the solar cell efficiency in the presence of hysteresis,^[37,38] but also for accurate parameter extraction in photodetectors, light emitting diodes, and hard radiation detectors.^[21] It has also been

recognized that the diversity of compositions and morphologies of halide perovskites, produces novel and unexpected responses. The modeling framework should provide the ability to analyze a broad range of techniques at the same time.

Meanwhile, the halide perovskites have found interesting applications in other research fields where the memory and hysteresis effects are a functional property, related to resistive switching and neuromorphic computation.^[39–43] The goal of neuromorphic engineering^[44,45] is to design and build artificial neural systems, like computational arrays of synapse-connected artificial neurons, and retinomorph vision systems.^[46] Memristors are highly nonlinear systems that show resistive switching under voltage cycling.^[47–50] Memristors for volatile memories can be switched between two states of conductance, with high and low resistance.^[51,52] To use a memristor as a synapse in a neural network, it is convenient to program it with distinct non-volatile resistive states that can support spike timing-dependent plasticity.^[47,53–56] Perovskite memristors, which show an amplified hysteresis property, in comparison with solar cells, are emerging as important candidates for the emulation of the brain functions with assemblies of artificial synapses and neurons.^[39,57–65] Using the remarkable photoexcitation properties of halide perovskites, photonic synapses are being investigated.^[64,66]

The combined study of perovskite solar cells and memristors has produced recently a useful class of models that are inspired by the biological formalisms that describe the temporal evolution of spiking neurons and the learning mechanisms of synapses.^[67–70] These “neuron-style” models enable a combined assessment of different responses such as the current–voltage curve at various scan speeds, the impedance spectroscopy, and the photocurrent transient to illumination. The model approach developed by our group and collaborators^[35,68,71–82] and other groups^[75,83] enables a very useful practical approach to the general dynamical properties of the complex coupled ionic-electronic response of perovskite devices. Based on this approach it has emerged a classification of hysteresis responses in terms of capacitive and inductive properties,^[84] that can be extended to a number of apparently unrelated devices, such as the organic electrochemical transistors, and the rectifying fluidic nanopores.^[84–86]

In this review, we describe the basic components of the neuron-style models applied to halide perovskite devices, and some of their properties in the standard kinetic measurement techniques. We present a systematic introduction of the different models and a unified approach that enables an understanding of the methods for their application in different types of situations. We use this approach to obtain insight into some key experimental aspects of the dynamical properties of halide perovskite devices.

Far from providing an exhaustive treatment of the enormous phenomenology of perovskite devices, here we show the main physical ideas, provide a representative example of applications, and indicate the relevant literature of several research directions.

As I have commented, this paper is about a specific modeling approach that has been developed mainly by the author and collaborators and a few other groups. However, we do not have any claim to the different experimental phenomena that the models address, and the physical explanations in terms of mechanisms, which have been obtained by a large number of scientists in an

enormous collective effort. I hope to highlight the main references where these contributions were presented, to the best of my knowledge. It is beyond our task and out of the scope to make a comprehensive account of all the publications where these varied phenomena have been discussed.

2. Dynamical Behavior of Halide Perovskite Solar Cells

This paper is strongly influenced by a large body of work on impedance spectroscopy of solar cells and memristors. As reviewed recently,^[87–91] the impedance is a powerful characterization tool that shows the dominant components of photoelectrical behavior in terms of resistances, capacitors and inductors, and how they are connected. As such, it provides an important dynamical picture of the device at a given operation point. The models can be well represented by an equivalent circuit that exposes the (often) complex processes going on. Equivalently, the same information can be analyzed by small steps or currents and voltage.^[92,93]

However, impedance spectroscopy and the associated equivalent circuit is a small perturbation response, and the need for more general approaches has emerged in relation to the realization that the impedance response is strongly connected to hysteresis types in large voltage scans of the current–voltage curves.^[84] This was motivated by the recognition of the connection of negative capacitance and inverted (inductive) hysteresis.^[28,94] In fact, the operation of solar cells and memristors in many circumstances requires to control the dynamical response to a large perturbation. Characteristic measurements are the following:

- i) A triangular voltage ramp formed by small step voltages, at scan rate S_r , used to measure the stationary current–voltage curve, by the scheme^[84]

$$V = S_r t \quad (1)$$

This is the essential method to measure the solar cell performance, whereby hysteresis becomes apparent.^[11–18]

- ii) Application of a large voltage step and measurement of current.^[95]
- iii) Application of a succession of large square voltage pulses in synaptical operation.^[60,62,73] The voltage pulses change the conductivity of the synapse element which is the memory property that is useful in the context of a neural network.
- iv) An illumination pulse or a succession of illumination pulses is used for the characterization of photodetectors.^[77,96–100] Related to this method is the open-circuit voltage rise or decay (OCVD) in which the open-circuit voltage is measured after disconnecting a stationary light source.^[7,10,101,102]

The application of complementary methods is a strong tool to obtain robust models and to reveal phenomena that can be hidden in one method and readily visualized in another, as shown by Ravishankar et al. for the charge extraction dynamics.^[103] Let us summarize the specific problems that we face in the analysis of important operational aspects of halide perovskite devices.

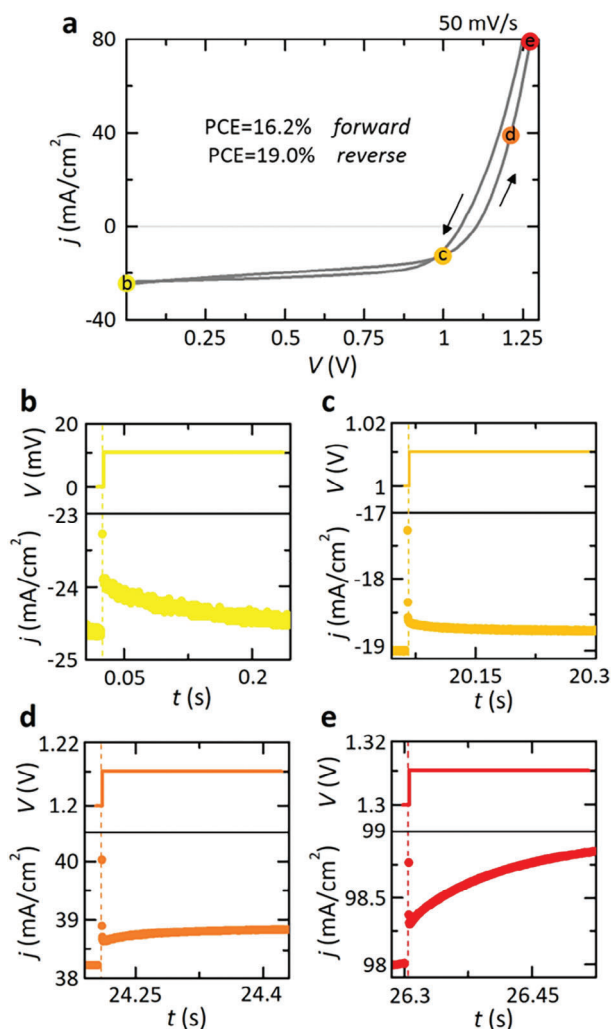


Figure 1. a) Representative current–voltage curve of a quadruple-cation perovskite solar cell with an active layer composition of $\text{Cs}_{0.05}\text{Rb}_{0.05}\text{MA}_{0.15}\text{FA}_{0.75}\text{Pb}_{1.05}(\text{Br}_{0.05}\text{I}_{0.95})_3$, obtained using a step-size of 10-mV and voltage scan rate of 50 mV s^{-1} . Halide perovskite exhibits normal and inverted hysteresis derived by the voltage-dependent transient dynamics of the photocurrent responses, consisting of decays at low voltages, b) 0 V and c) 1 V, and negative spike components with abrupt final rises in current for the high voltage-domain, d) 1.2 and e) 1.3 V. H. Reproduced with permission^[72] Copyright 2024, Creative Commons Attribution (CC BY 4.0) license:

In **Figure 1** we show characteristic measurement of the current–voltage curve under illumination of a PSC. The curve shows a separation when forward and backward directions are recorded, which is the often-found phenomenon of hysteresis. This effect complicates the evaluation of performance. Furthermore note that there is a self crossing point (c), where the hysteresis changes from capacitive at lower voltage, to inductive at higher voltage.^[72,84] Correspondingly, the small signal transient photocurrent is also observed to change qualitatively. After an initial fast spike, the longer time dynamics decrease with time in the capacitive region (b), and increasing with time in the inductive re-

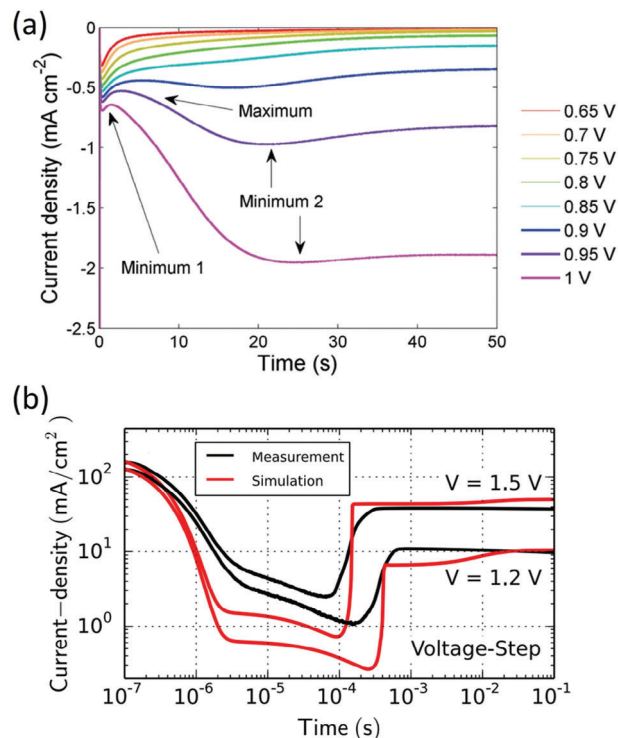


Figure 2. a) Experimental evolution of current transients in response to steps from 0 V to different values of voltage for a perovskite solar cell with configuration FTO/TiO₂/MAPi (MAPbI₃)/spiro-OMeTAD/Au cell. Time transient with inductive loop traces appears at voltages values >0.9 V. Reproduced with permission^[95] Copyright 2017, Creative Commons Attribution (CC BY 4.0) license. b) Measurement (black) and simulation (red) of transient currents as a response to voltage steps in the dark in the log-log representation for a device structure as ITO/TaTm:F₅-TCNNQ/TaTm/MAPi/C₆₀/C₆₀:PhIm/Ag. Reproduced with permission^[104] Copyright 2019.

gion (e). The combination of initial decay and long term current increase is shown in **Figure 2** for large perturbation voltage steps.

These dynamical effects have important implications. For establishing the performance in terms of the power conversion efficiency (PCE) it is necessary to obtain the product of current and voltage at the maximum power point (MPP). It is required to apply time-consuming advanced measurement protocols such as MPP tracking.^[37,38,36,105–107] These methods are generally based on a perturb-and-observe algorithm. The power output is maximized by constantly perturbing the operating voltage and recording its effect on the power output until the convergence is satisfied. In the area of PSC it has been understood the connection between the impedance components and the hysteresis behavior,^[17,108–112] with important application for stabilization of the current–voltage curves and determining the stationary performance. The large capacitance of the PSC^[17,26,110,112,113] interferes with the convergence of the tracking algorithm.^[19] **Figure 3** shows the different steps of the current–voltage curve, in (a–f), that in this case shows a capacitive transient response. The oscillations leading to stabilized performance are shown in **Figure 3f,g**. Determining the MPP requires some oscillation to the steady state situation, that present a complex relationship with the maximum output point, and as shown in **Figure 3f** the

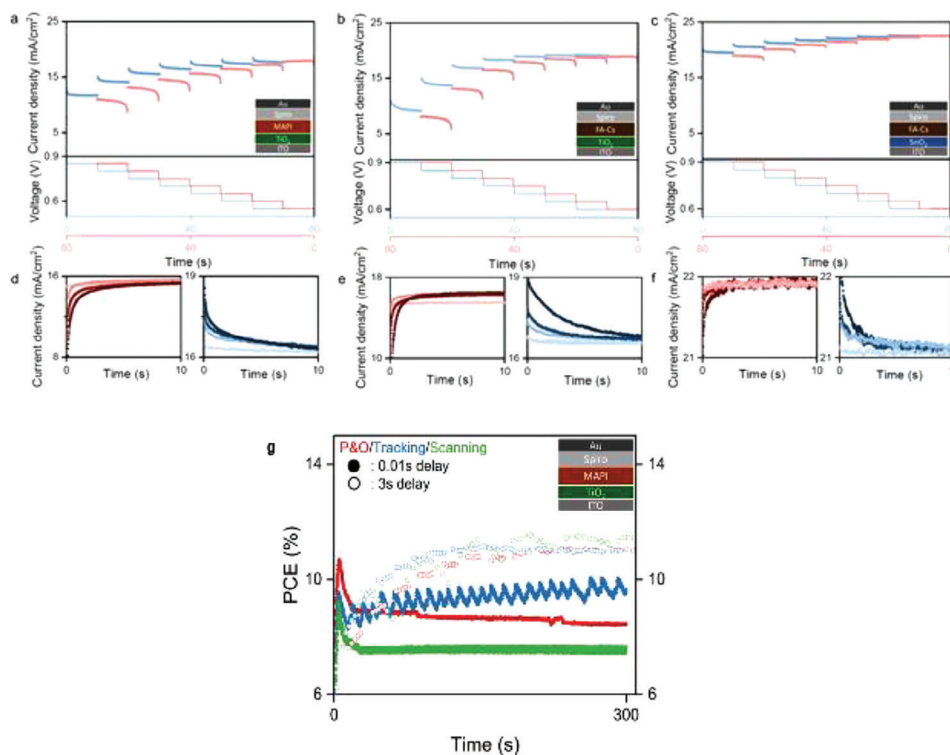


Figure 3. Exponential transient current density measurement for a–c) voltage stepping in SC-OC and OC-SC directions and d–f) detailed transient current density response at 0.9 V for the different voltage step sizes (light to dark color: 0.01, 0.05, 0.1, 0.2 V) for SC-OC (red) and OC-SC (blue) stepping. studied solar cells use either MAPI or $\text{Cs}_{0.1}\text{FA}_{0.9}\text{PbI}_{2.865}\text{Br}_{0.135}$ (FACs). Three different stacks: (a/d) TiO_2/MAPI (b/e) TiO_2/FACs (c/f) SnO_2/FACs . g) MPP tracking for the different algorithms used on the same cell on TiO_2/MAPI PSC using measurement delays of 0.01 s (closed dots) and 3.0 s (open dots). Reproduced with permission^[37] Copyright 2019.

determined performance may depend on the method used. In general, if hysteresis causes significant transient behavior at the given chopping frequency then there is concern to determine the performance parameters.^[19] Sophisticated tracking methods have been developed to ensure the convergence.^[114]

Clearly, the transient behavior is the key for establishing the stabilized performance in a reasonable time^[72] thus ref. [37] includes the measuring of the transient time to the tracking method. The direction of convergence will be inverted if the hysteresis is changed. ref. [19] suggested the incorporation of a hysteresis tracker to the algorithm, and ref. [72] provides a criterion based on the transient behavior to determine the maximum scan rate at which hysteresis vanishes. This method will be explained in Section 15.

3. Basic Solar Cell Device Model

There is a good general understanding of photovoltaic models.^[117,118] The incident light produces a generation of electrons and holes, that cause a splitting of the Fermi levels which is opposed by internal recombination, determining a photovoltage V_{oc} . The charge extraction at selective contacts creates a photocurrent j_{ph} . These models, based mainly on standard semiconductor properties, cover well the main photovoltaic technologies, such as silicon and thin film solar cells.^[119] Other types of devices, like the dye-sensitized solar

cells and the organic solar cells,^[120] require some electrochemical concepts related to ion transport and a visible chemical capacitance.^[121,122]

Very often the aim of characterization of solution-processed solar cells was on the detailed understanding on transport and recombination conditions, in order to improve the performance. This method enables optimization of the material parameters of a specific configuration. One could devote a large effort to the detailed understanding of a single device and make an interesting publication. This attitude is still applied for PSC, by using a range of measurement methods and explaining significant details of the deviation from the maximal theoretical performance.^[123]

However, as the PSC research progresses, other needs have emerged. One must take into account the extraordinary variety of compositions^[124,125] and morphologies^[126] that can be explored. For technological progress it is necessary to evaluate the performance and degradation under ageing of thousands of devices.^[19,38] There is scope for unified methods that can evaluate dynamical properties of devices with rather different behavior, from nearly steady state operation, to ultrafast switching behavior. The general purpose of reviewing here neuron-style models is to encourage methods that provide significant insight into device dynamical properties with relatively low numbers of parameters, which allows the comparison of different types of devices.

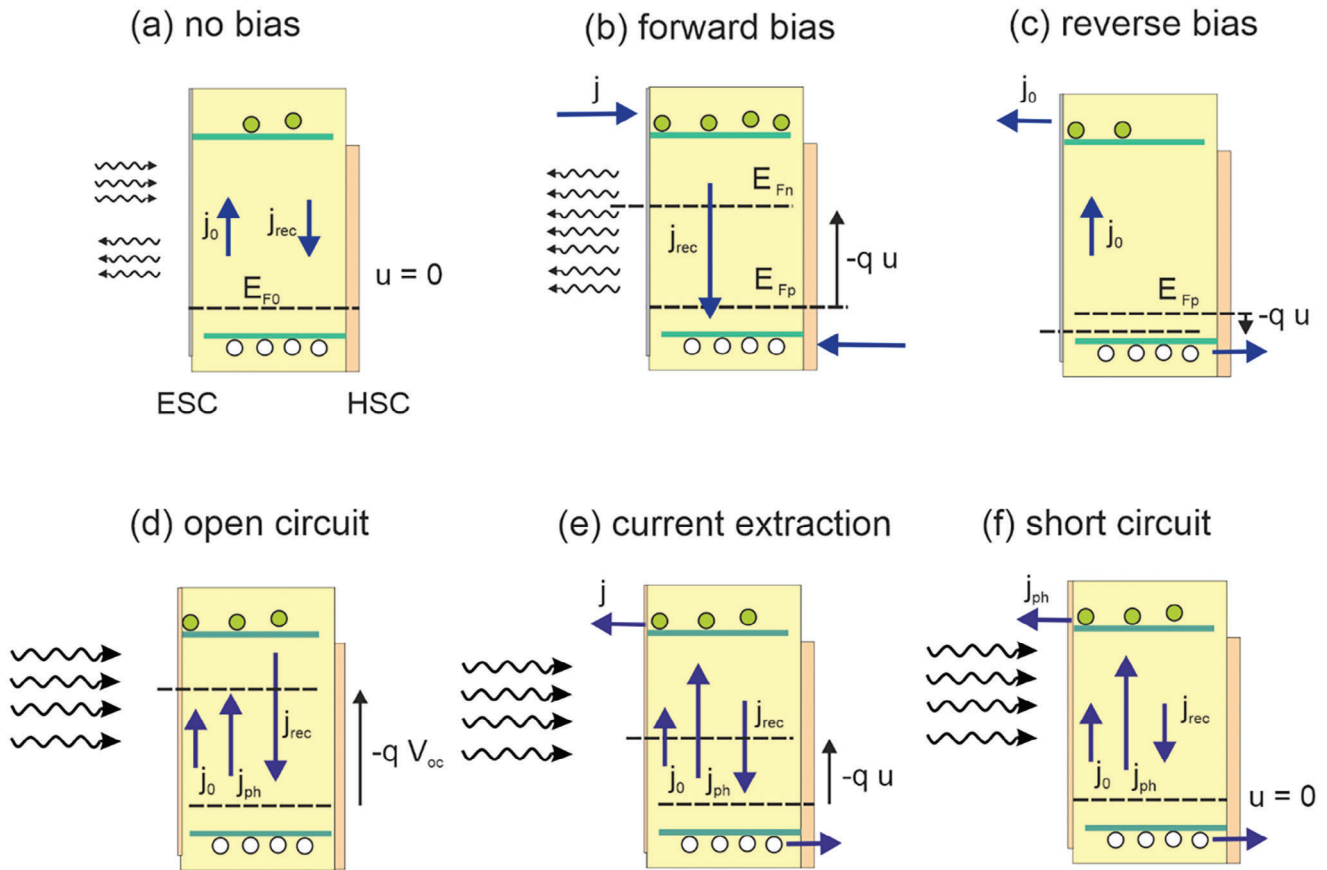


Figure 4. a) Scheme of p-type semiconductor material with selective contacts to electrons and holes, ESC and HSC, a model of a solar cell. a–c) In dark, is the dark generation current (by incoming photons) that coincides with the diode reverse saturation current. is the recombination current that generates outgoing photons (neglecting photon recycling effects). a) In dark equilibrium, showing the balance of incoming and outgoing photons absorbed or produced in the material, and the equilibrium Fermi level. b) At forward bias, the minority carrier electrons Fermi level increases and current is injected at the contacts. c) At reverse bias, the carriers are extracted determining the reverse saturation current. d–f) Under illumination, absorbed photons promote excitation of electrons from the valence band to the conduction band. d) Open circuit: The generation current achieves equilibrium with recombination. This raises the electron Fermi level and causes the production of the photovoltage. No current is extracted from the solar cell. e) At lower voltage than, the recombination rate is less than the total generation, electrons and holes are extracted in the external circuit and this constitutes a photocurrent. f) Short-circuit: The voltage is zero, all the current created by photogeneration from the illumination in excess of thermal radiation is extracted and constitutes the short-circuit current.

With these objectives in mind we introduce in **Figure 4** a suitable photovoltaic model based on fundamental principles. This model has been explained in detail in my book^[127] and a brief summary is presented here. This simple model has the advantage that contains the essential elements of photovoltaic operation, and the limitations of the model will be pointed out and improved later on.

The device is formed by the light-absorbing semiconductor containing electrons and holes, with densities n , p , and Fermi levels E_{Fn} , E_{Fp} , respectively. The voltage in the solar cell is defined as u and is related to the separation of Fermi levels at the complementary selective contacts, as:

$$u = \frac{E_{Fn} - E_{Fp}}{q} \quad (2)$$

where q is the elementary charge. The meaning of analytical variables is summarized in **Table 1**.

Recombination of electrons and holes at position x occurs with the rate $U_{rec}(n, p, x)$. The recombination current density j_{rec} is defined as the integration across the film thickness L

$$j_{rec} = \int_0^L U_{rec}(n, p, x) dx \quad (3)$$

The top line in **Figure 4** identifies the dark operation. The semiconductor material is bathed in the Lambertian blackbody radiation that generates a flux of generated electrons termed j_0 . In **Figure 1a** the dark generation in equilibrium is balanced by the recombination current. Therefore

$$j_0 = j_{rec} (u = 0) \quad (4)$$

In forward bias, carriers are injected to the semiconductor. Recombination increases exponentially, according to the

Table 1. Notation.

V	Applied voltage
V_{oc}	Open circuit photovoltage
V_{bi}	Built-in voltage
u	Internal voltage
v_s	Slow internal surface voltage
n_r	Bulk diode recombination ideality factor
n_s	Surface diode recombination ideality factor
n_r	Effective diode recombination ideality factor $\frac{n_r n_s}{n_r + n_s}$
j_{tot}	Total external current density
j_{ph}	Photocurrent density
$J_{rec}(u)$	Stationary recombination current density $J_{rec0} e^{\frac{qu}{k_B T} \frac{u}{n_r}}$
$j_{rec}(u, v_s)$	Recombination current $J_{rec0} e^{\frac{q}{k_B T} (\frac{u}{n_r} + \frac{v_s}{n_s})}$
j_d	Slow internal current
C_s	Surface capacitance $C_{s0} e^{\frac{q}{k_B T} \frac{v_s}{n_s}}$
g_s	Differential conductance $\frac{q}{n_s k_B T} J_{rec}(u)$
g_r	Differential conductance $\frac{q}{n_r k_B T} J_{rec}(u)$
g_C	Differential conductance $\frac{C_s}{\tau_s}$
τ_a	Capacitive time constant $\frac{C_s}{g_s}$
τ_s	Inductive time constant $g_s L_s$

parameter n_r , the recombination diode quality factor. The recombination current is then written as:

$$j_{rec} = j_0 e^{qu/n_r k_B T} \quad (5)$$

Here k_B is the Boltzmann's constant and T the absolute temperature. Usually, n_r takes values between 1 and 2. As discussed later the analysis of the diode factor requires a careful assessment of the ideality factor of the different resistances in the system, in order to identify the origin of recombination mechanisms.^[128] These properties are investigated in recent publications.^[29,128–133]

In *steady state*, the net current extracted from the diode is:

$$j_{tot} = j_{rec} - j_0 \quad (6)$$

The carrier densities are homogeneous across the solar cell thickness due to fast transport so that the bands and the Fermi levels are flat. The current density–voltage characteristic, takes the form

$$j = j_0 (e^{qu/n_r k_B T} - 1) \quad (7)$$

Note that j_0 is the same parameter as the reverse saturation current of the diode equation.

When illumination impinges the device, the carrier generation produces a photocurrent, j_{ph} . The lower row of Figure 4 shows the three important conditions of the solar cell regulated by the voltage applied externally. At open circuit (OC) no current leaves the device. At intermediate voltage the extracted current is:

$$j_{tot} = -j_{ph} + j_0 (e^{qu/n_r k_B T} - 1) \quad (8)$$

Finally at short circuit $u = 0$ and the full photocurrent is extracted.

The model of Equation (8) provides a suitable starting point for the transient behavior of PSC, as discussed later. This model allows to characterize the dominant internal carrier density in terms of the internal voltage. Some comments are needed to qualify the application of this framework.

Figure 5 shows a more detailed modeling showing the evolution of the charge densities into the transport layers. However, it must be noted that the Fermi levels are nearly flat as suggested in the homogeneous model. This is due to the fact that the solar cell has a large charge collection efficiency, related to fast transport characteristics. We can observe that at low voltage in Figure 5b the different cells show a similar behavior where the decrease of the voltage makes very little effect on the photocurrent. A similar behavior is observed in Figure 1a. It is close to V_{oc} where the interesting action occurs, which means that the internal electrical field can be ignored and the cell operates basically by recombination effects. Figure 5c shows results of a single junction PSC that yields 27% efficient monolithic n–i–p perovskite/silicon tandem solar cells. In this optimized device the current–voltage curve is practically flat close to SC, and there is almost no hysteresis below $0.5 V_{oc}$, while capacitive hysteresis is observed close to V_{oc} . The hysteresis is well correlated with the results of impedance spectroscopy shown in Figure 5d.

This is when the model by Equation (8) is appropriate. Furthermore, we can ignore the term j_0 , as it is only significant in reverse voltage. Henceforth we use uppercase letter for the stationary recombination current and we have

$$J_{rec}(u) = J_{rec0} e^{\frac{qu}{n_r k_B T}} \quad (9)$$

$$j_{tot} = -j_{ph} + J_{rec}(u) \quad (10)$$

As the photocurrent is an added constant in this approach, the subsequent models will focus on the recombination current.

In some PSCs, there may be charge collection issues, and the influence of the electrical field formed by ions in the photocurrent has been adopted for interpretation of hysteresis effects.^[104,135,136] In devices as photodetectors, that do not have intrinsic charge collection, the effect of electrical field on the photogenerated carriers needs to be considered. These effects will be discussed in Section 11.

4. Halide Perovskite Memristor Devices

We turn our attention to a different type of halide perovskite device, normally termed a memristor, with examples shown in Figures 6–9. These devices are intended for brain-like computation networks and memory storage as commented in the Introduction.^[138,139] We observe that the dark current–voltage characteristics in Figures 6–9 resemble those of the solar cell devices. However, the significant difference is a huge hysteresis loop that is onset at some positive voltage. This loop represents the property of resistive switching between a low and a high conductance state. In some cases, the rising current obtains an exponential dependence, so that these devices can still be regarded as controlled by recombination as in Equations (9) and (10). The detailed mechanisms are often complex, as indicated Figure 7. In classical memristors the resistive switching corresponds to the construction of a conducting ionic filament in an insulating

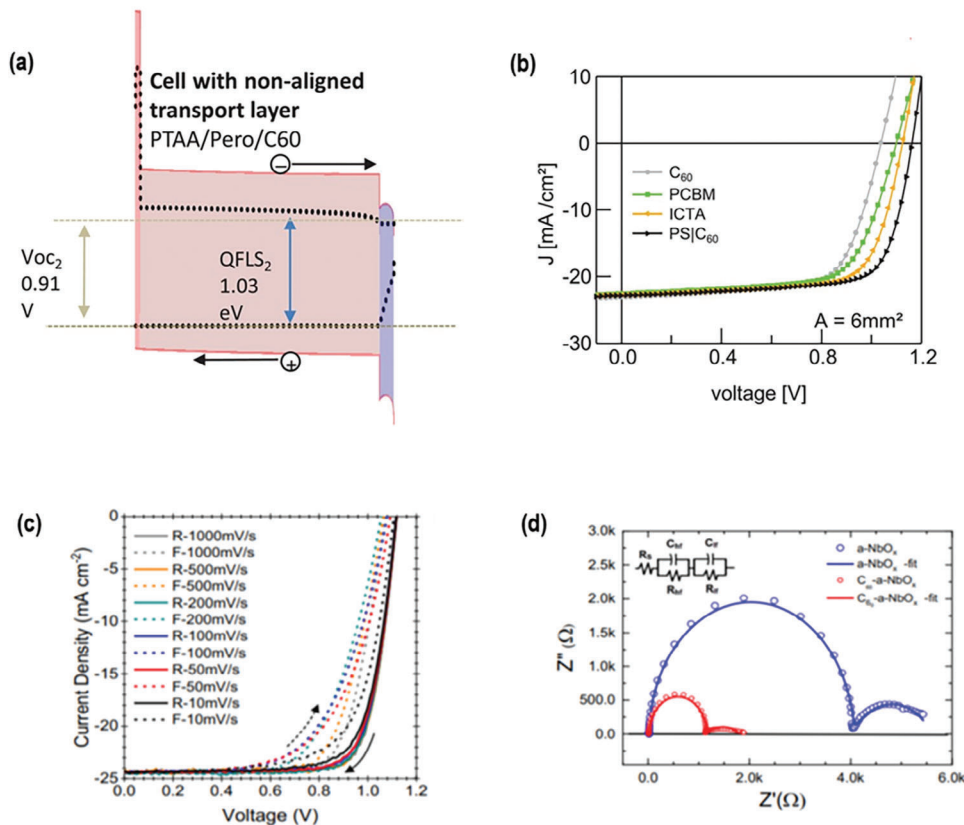


Figure 5. a) Device simulations of perovskite cells (ITO/PTAA/perovskite/C₆₀/BCP/Cu) with and an energy offset of 0.3 eV at the perovskite/C₆₀ interface which leads to considerable V_{oc} loss of 0.27 V (from 1.18 to 0.91 V) due to a built-up of charge carriers at the electron selective contact, which increases the interfacial recombination. b) The J–V curves of the corresponding p-i-n devices demonstrating the improved V_{oc} from C₆₀ to PCBM to ICTA to PS/C₆₀. Reproduced with permission^[130] Copyright 2019. c) Hysteresis analysis of single-junction solar cells. Influence of the voltage scan speed on the hysteresis behavior of the C₆₀-anchored a-NbO_x based PSCs based on 1.61 eV perovskite absorbers. d) Impedance analysis of the a-NbO_x and C₆₀-anchored a-NbO_x contacts at V_{oc} condition under 0.01-sun illumination. Reproduced with permission^[134] Copyright 2021, Creative Commons Attribution (CC BY 4.0) license.

medium,^[140,141] or the modification of interfacial barriers.^[142] In the halide perovskite memristors, the blocking medium may be a thin insulating buffer layer at one contact, as in Figure 7,^[137] and the onset voltage depends critically on the metal contact and ionic distributions.^[143,144] These complex multi-ionic chemical processes require a first conditioning cycle Figure 7c, before establishing the stabilized operation, which may consist on the combination of successive onset processes. Note in Figure 6 that the device shows a change of property from capacitive hysteresis at low voltage to inductive hysteresis at high voltage, similar to that in Figure 1a.

The application of halide perovskite memristors for computational networks relies on the change of the conductance state, associated to the inductive hysteresis, that is shown in Figure 8. The gradual rise of current level by a train of voltage pulses is termed potentiation, as it will increase the weight of a synapse by the received positive signal, or the opposite case in depression. Figure 9c,d show the detailed transient behavior, that is composed of a fast initial spike, and a current increase at longer time. These are the trends already remarked in Figure 2 but more clearly defined. These features, described in Section 14, are closely related to the capac-

itive and inductive hysteresis observed in the current–voltage curves.

5. The Biological Neuron Response

Beyond the steady state effects represented by Equations (9) and (10) we aim to introduce the dynamical effects in order to explain the results of measurements summarized in Section 2. In order to set the precedents of the models developed later, we explain first the neurological model, then the engineering idea of a memristor, and also the definition of a chemical inductor.

For emulating the physical behavior of neurons and synaptic devices, one takes advantage of the knowledge about the natural systems. Neurons convey information via spiking signals, characterized by their sparse, pulsed, and frequency-modulated nature. These spikes originate from voltage-gated ion channels within the neuron membrane, shown in Figure 10a. By a coupled operation of these channels, the neuron emits trains of single-bit impulses called action potentials, Figure 10b, which are then transmitted to neighboring neurons through synapses.^[145,146]

Around 1950 Hodgkin and Huxley (HH) developed a model, based on a set of differential equations.^[145,149–151] A range of

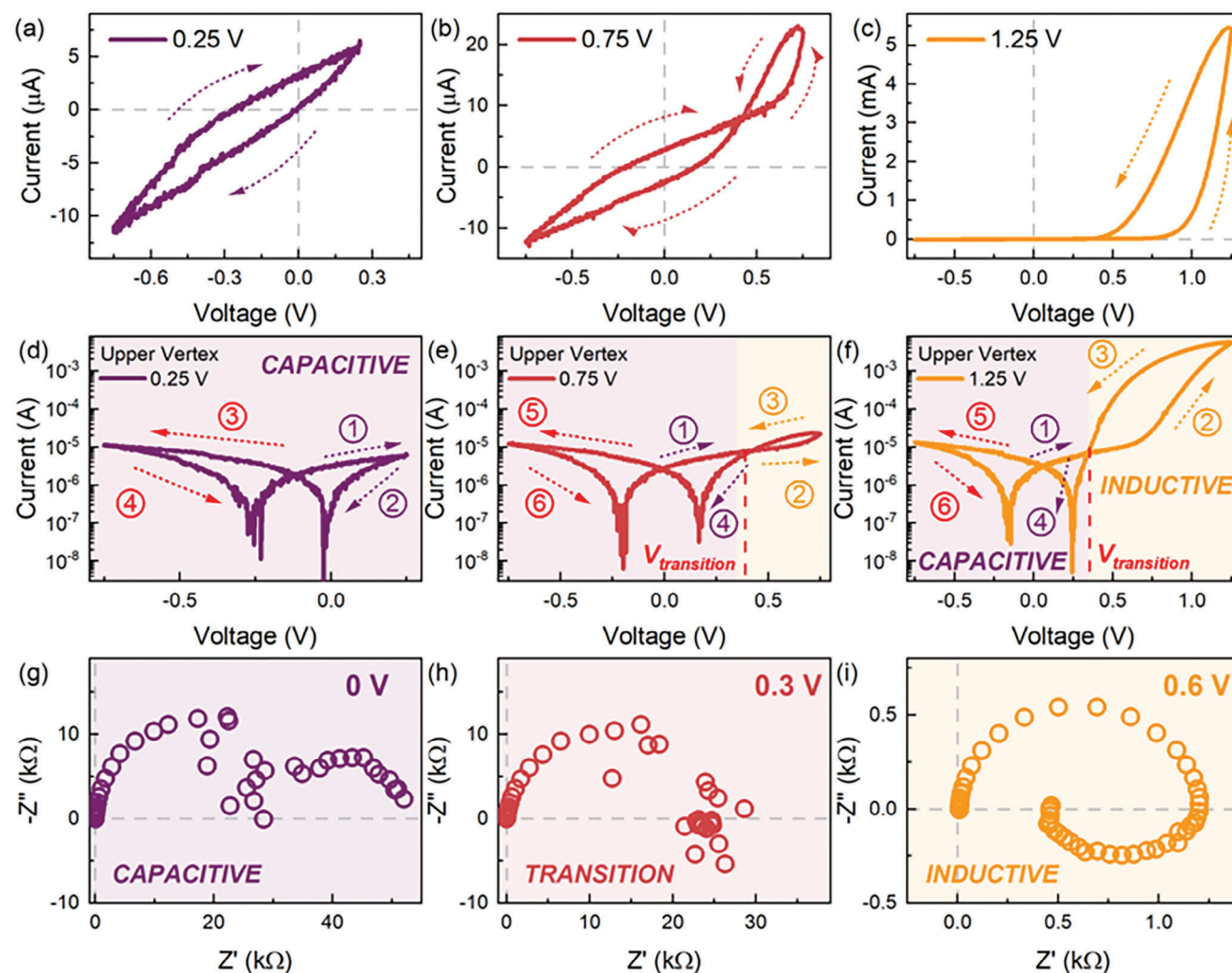


Figure 6. Characteristic current–voltage (I – V) response in the linear scale of the FTO / PEDOT:PSS/MAPbBr₃ / Au memristor device with varying upper vertex voltages of a) 0.25, b) 0.75, and c), 1.25 V, with the arrows indicating the scan direction. Corresponding I – V response in the semi-log scale for upper vertex voltages of d) 0.25 V, e) 0.75, and f) 1.25 V with the arrows and numbers indicating the scan direction and sequence, respectively. Voltage-dependent impedance spectral evolution measured at g) 0 V, h) 0.3 V, and i) 0.6 V exhibiting a transition from a low frequency capacitive response at low applied voltages to a low frequency inductive response at high applied voltages. Figure courtesy of Cedric Gonzales. Reproduced with permission^[84] Copyright 2023, Creative Commons Attribution (CC BY 4.0) license.

bio-physical models extended the original HH formulation^[145,152–156] incorporating different types of complexities that enable the realistic simulation of neural systems. The enormous success of HH model is due to the accurate representation of the concerted operation of the ion channels, that describes well the temporal responses of action potentials illustrated in Figure 10.

Consider the voltage u and the current j_{tot} across the neuron wall. The structure of the HH model is as follows:

$$j_{tot} = C_m \frac{du}{dt} + g_{Na} m^3 h (u - E_{Na}) + g_K n^4 (u - E_K) + g_{leak} (u - E_{leak}) \quad (11)$$

$$\tau_m(u) \frac{dm}{dt} = M(u) - m \quad (12)$$

$$\tau_h(u) \frac{dh}{dt} = H(u) - h \quad (13)$$

$$\tau_n(u) \frac{dn}{dt} = N(u) - n \quad (14)$$

The first term in Equation (11) is a capacitive charging with the capacitance C_m of the neuron wall. The next three terms correspond to generalized Ohm's law where $(u - E_i)$ is the driving force. Each type of channel is selective to conduct one type of ion, with conductance g_{Na} , g_K , g_{leak} where the latter is a leak term, and the E_{Na} , E_K , E_{leak} are the equilibrium potentials at which each of the currents is balanced by ionic concentration differences across the membrane. The variables m , h , n , vary between 0 and 1 and represent sodium channel conductance activation, sodium channel deactivation, and K channel activation respectively. These

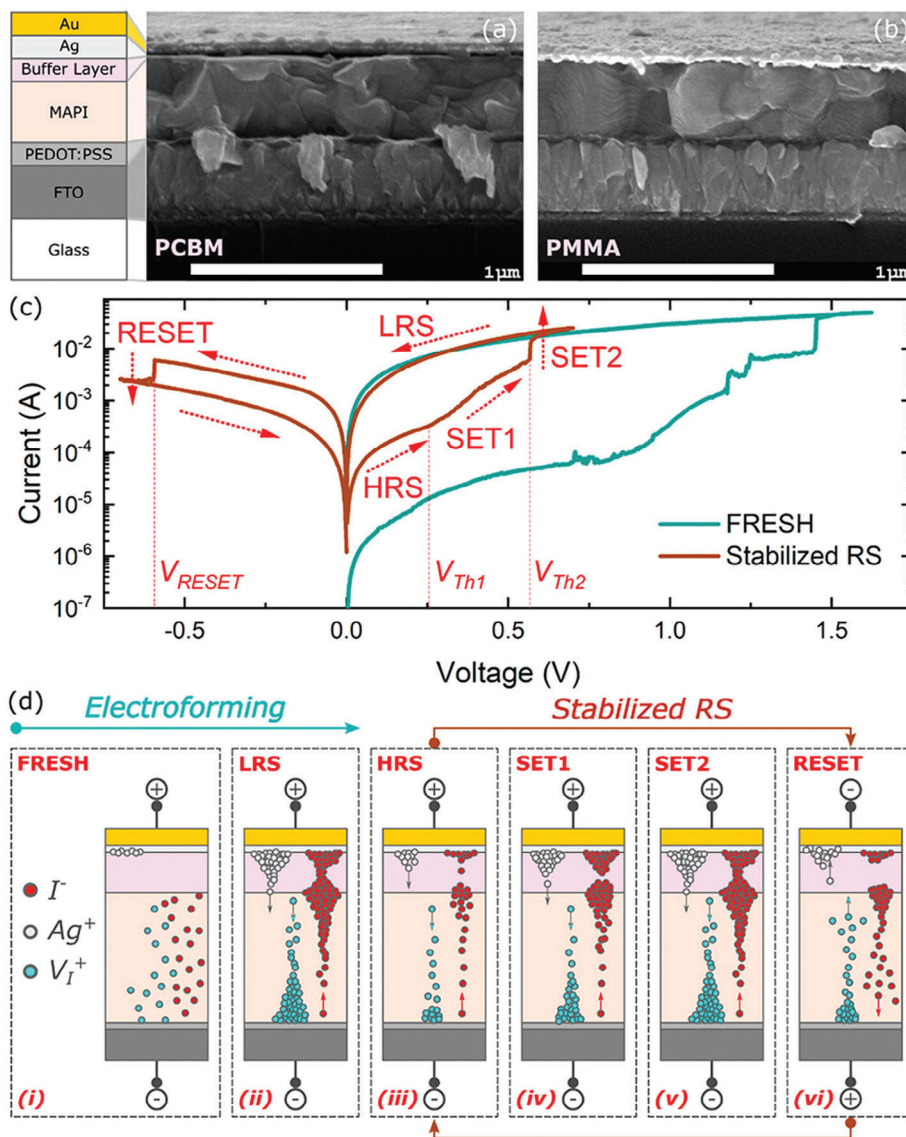


Figure 7. Cross-sectional SEM micrographs of MAPbI₃ memristors with thin undoped a) PCBM and b) PMMA buffer layers with a schematic diagram of the device configuration. c) Representative characteristic I–V curves of the initial conditioning step of the FRESH device and the stabilized two-step SET process and RESET process with the arrows indicating the scan direction. d) Schematic diagram of the electroforming and two-step SET process mechanism under the applied voltage of the memristive devices with buffer layers. The colors of the device configuration indicate the layers in the schematic diagram. Reproduced with permission^[137] Copyright 2023, Creative Commons Attribution (CC BY 4.0) license.

variables describe the conductance state of each channel according to the kinetic relaxation Equations (12–14). The kinetic times τ_m , τ_h , τ_n are a function of the voltage u , and so are the equilibrium functions M , H , N of the activation variables. Detailed interpretation of these mechanisms and their applications to artificial neurons is explained in ref. [67].

6. Simple Memristor Model and the Chemical Inductor

The observation of resistive switching goes back in the centuries and resistive switching technology is continuously investigated for different types of applications.^[51,157–159] In recent decades,^[160]

following Chua's suggestion these systems have been broadly conceptualized as memristors.^[52,161] Memristors can be defined as a nonlinear system with memory affected by one or more state variables denoted x_i .^[48]

$$j_{tot} = F(u, x) \quad (15)$$

$$\tau_k \frac{dx}{dt} = X_{eq}(u) - x \quad (16)$$

Equation (15) is a conductance equation that depends on the voltage u and a state variable x . The adaptation of x to the equilibrium value $X_{eq}(u)$ is delayed by the Equation (16) with the

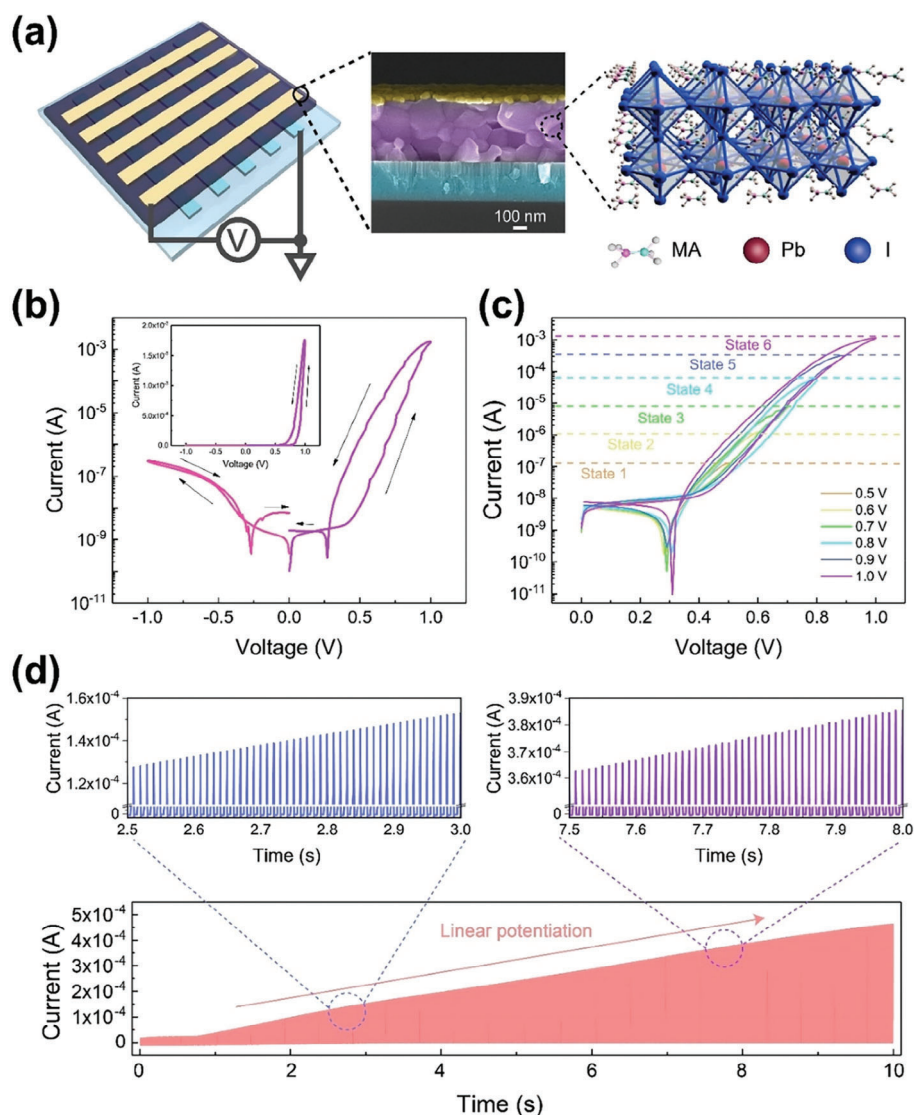


Figure 8. Electrical Performances of the halide perovskite-based memristor. a) Schematic illustration of the fabricated Au/MAPI/ITO memristor (left), cross-sectional SEM image of the memristor (middle), and molecular structure of MAPI (right). b) Typical I – V characteristic of the memristor. (inset: I – V characteristic under linear coordinate.) c) I – V characteristic with different sweeping voltages ranging from 0.5 to 1.0 V. d) Demonstration of the linear potentiation of the device's conductance with 1000 continuous impulses. Upper left: an enlarged picture of current trend between 2.5 and 3.0 ms. Upper right: an enlarged picture of current trend between 7.5 and 8.0 ms. ($V_{\text{pulse}}=2$ V, $V_{\text{base}}=0$ V, $T_{\text{pulse}}=5$ ms, $T_{\text{interval}}=5$ ms). Reproduced with permission^[61] Copyright 2020, Elsevier.

relaxation time τ_k . Several examples of the memory variable will be classified below.

Solar cell devices usually have a series resistance R_s so that the applied voltage V is divided as:

$$V = R_s j_{\text{tot}} + u \quad (17)$$

where j_{tot} is the current density and u is the voltage inside the device, as mentioned earlier. The voltage in the series resistance is an important factor when the potentiostatic impulses are applied to the solar cell.

By the normal usage of “memristor”, the phenomenon of resistive switching is understood, and in fact many authors reserve

this denomination for devices that show permanent, non-volatile distinct resistive states.^[49] However the memory mechanism in Equations (15) and (16) is of much broader scope, and applies in many systems unrelated to the resistive switching. This mechanism has been given the general denomination of a chemical inductor,^[69,162] with applications in diverse fields as electrocatalysis, batteries, neurons, and solar cells.^[67,162] The relaxation Equation (16) is suggested in mechanisms of the negative capacitance in electrochemistry^[163–165] and in bulk polarization models.^[83]

As an example, we remark that the HH model of Equations (11)–(14) have the structure of three chemical inductors by the activation variables m , h , n . To my knowledge, HH model is the first application of a chemical inductor in any area of science.

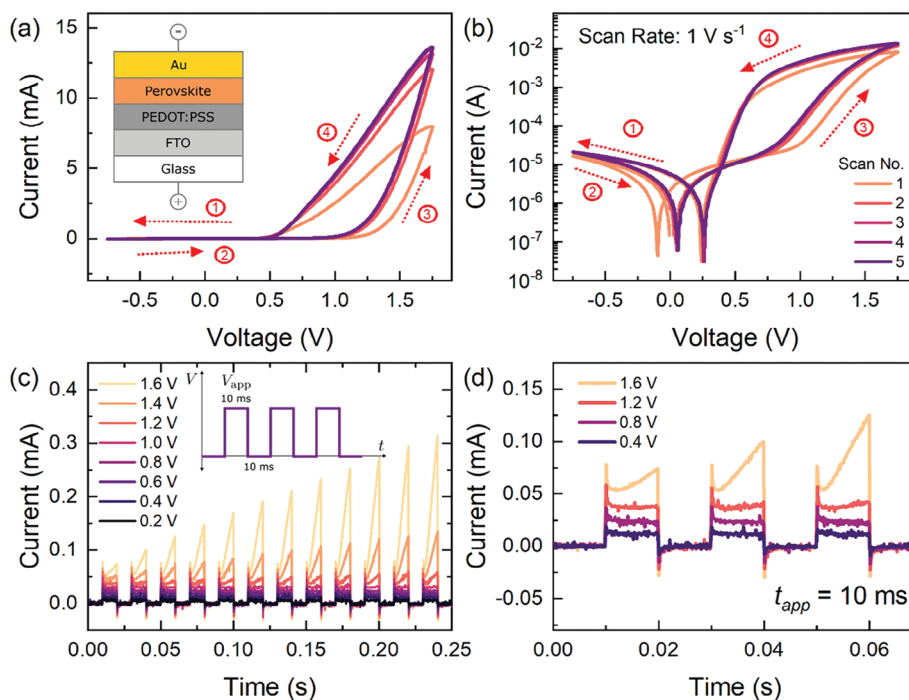


Figure 9. a) The characteristic I – V response in the linear scale of the FTO / PEDOT / MAPbBr₃ / Au device with the inset illustrating the schematic diagram of the device configuration, b) the characteristic I – V response of the perovskite device in the semi-log scale with the arrows and numbers indicating the scan direction, c) the transient current response of the device at varying applied voltages (V_{app}) from 0.2 V to 1.6 V with the inset indicating the applied voltage pulses, and d) the transient current response of the first three voltage pulses at representative applied voltages. Reproduced with permission^[77] Copyright 2023, American Chemical Society.

This structure is unrelated to resistive changes, instead, it can be regarded as a voltage-gated ion channel, that produces the repetitive spiking shown in Figure 10. This voltage gating has also been applied to describe the dynamics of PSC.^[79]

Making artificial neurons is of great interest for brain-like computation. As reviewed recently in ref. [67], the spiking in Figure 10 requires an additional feature not included in normal chemical inductors. This is a negative conductance effect, that causes a Hopf bifurcation in which the system enters an out-of-equilibrium state in which permanent oscillations forming repetitive action potential patterns occur.^[166,167] The neuron spiking by a negative resistance has been demonstrated by the decreasing mobility at higher bias voltage in electrochemical transistors.^[147,168] This topic of artificial neurons will not be further considered in the present work.

To start the application of neuron-style models to the halide perovskite devices, we explain different models that have the structure of the chemical inductor (or memristor) model in Equations (15) and (16) with various physical interpretations.

7. Slow Recombination Effects: The Delayed Surface Voltage

The first model we present is a generalization of the basic solar cell model of Equations (9) and (10) as follows:

$$j_{tot} = C_g \frac{du}{dt} + j_{rec}(u, v_s) \quad (18)$$

$$\tau_s \frac{dv_s}{dt} = u - v_s \quad (19)$$

We have included in Equation (18) the capacitive current, as in Equation (11), due to a geometric capacitance C_g . We observe in Equation (18) that the recombination current $j_{rec}(u, v_s)$ depends not only on the instantaneous applied voltage u , but also in a surface voltage v_s that is the internal state variable in this model.

The rationale for this model started in the observation of significant changes of the OCVD by previous illumination as shown in Figure 11.^[7] The illumination causes a change of surface charge distribution by mobile ions that become sluggish under dark conditions. An excess potential that we term here v_s , is trapped at the interface. Equations of the type (18–19) were proposed in the surface polarization model (SPM).^[115,116] The relaxation time τ_s can be interpreted in terms of the internal ionic dynamics,^[7] corresponding in some cases to equilibration by ionic diffusion.^[85]

The excess surface voltage produces an excess surface charge that influences recombination in the solar cell, as shown in Figure 12. To describe both components of recombination we use the expression^[116]

$$j_{rec}(u, v_s) = J_{rec0} e^{\frac{q}{k_B T} \left(\frac{u}{n_r} + \frac{v_s}{n_s} \right)} \quad (20)$$

Here we employ two different ideality factors: n_r is for the bulk recombination, and n_s for the surface recombination. According to Equation (19), in equilibrium, or in a slow measurement with

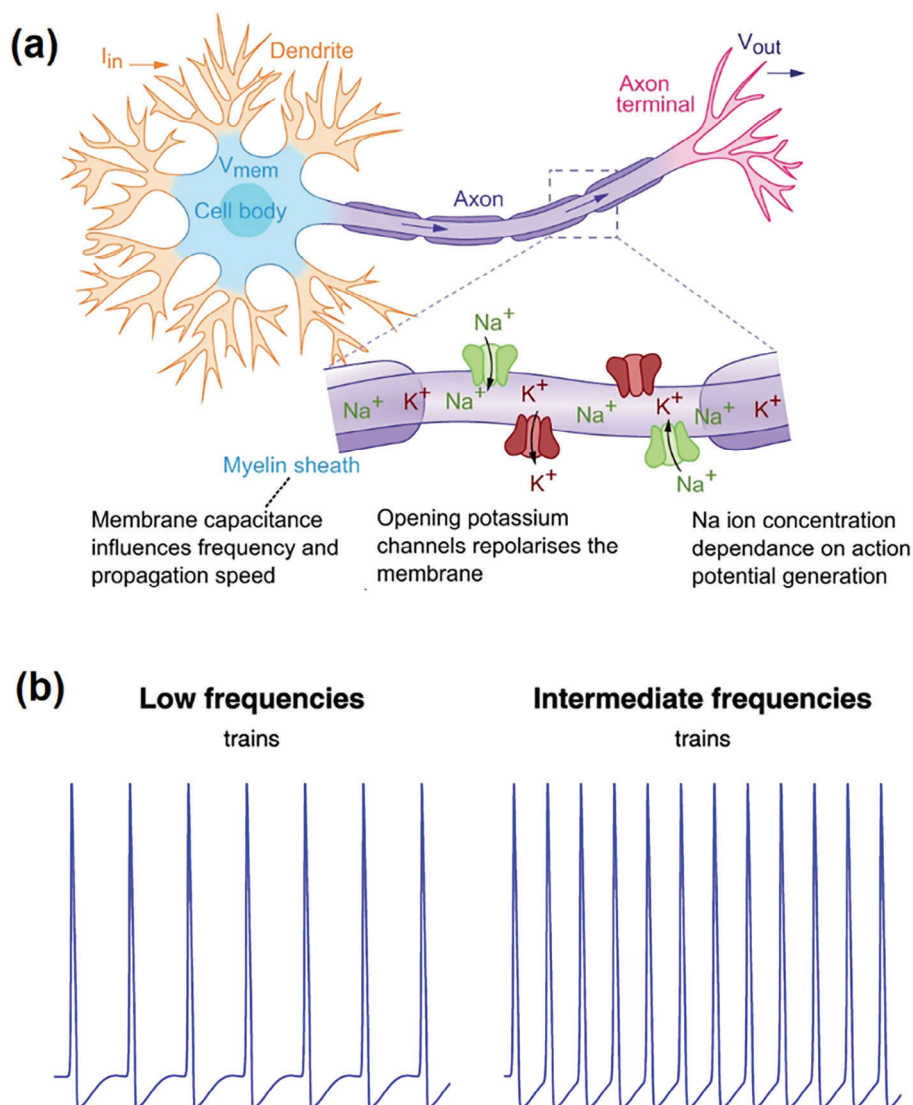


Figure 10. a) Schematic of the biological neuron. Reproduced with permission^[147] Copyright 2022, Creative Commons Attribution (CC BY 4.0) license. b) Representative responses to current stimuli along axons calculated by Hodgkin-Huxley model. Reproduced with permission^[148] Copyright 2017, Creative Commons Attribution (CC BY 4.0) license.

respect to the timescale τ_s , we have $v_s \rightarrow u$, hence Equation (20) becomes Equation (9), with the effective ideality factor

$$n_r = \frac{n_\tau n_s}{n_\tau + n_s} \quad (21)$$

The slow equilibrium current is shown in gray in Figure 13. If, however, we perform a very fast measurement, then the surface potential cannot respond, and remains stuck at some value, say $v_s = 0$. Then we get the blue curve of Figure 13.

Consider next that we operate at finite velocity a forward and reverse cycle as Equation (1). Then the curve in Figure 13 is obtained in which the forward current is smaller than the reverse current. This is the famous inverted hysteresis^[71,111,169] that here we term also inductive hysteresis.^[84] It has the property that the

largest the scan rate, the more the forward current will approach the limiting blue line (because the slow recombination mode cannot be activated).

In Figure 13 the capacitive effect is neglected. If the capacitance is dominant, then the converse direction of the cycle occurs, in which the forward current is larger than in reverse.^[15,71,84] The capacitive hysteresis will be illustrated later on.

8. Impedance Spectroscopy Model

For a better understanding of the dynamical properties underlying the features in Figure 13 we explore the response of the system under a linear perturbation. This analysis shows some general properties shared by all the chemical inductor models, that will be obtained from Equations (18–19).

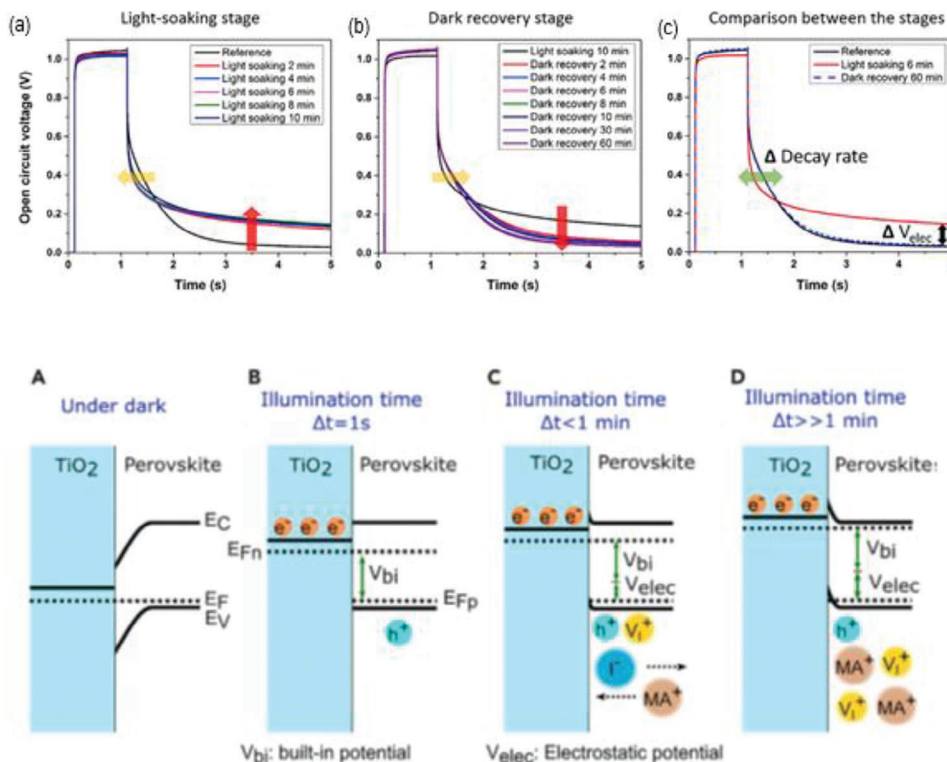


Figure 11. a–c) Open-circuit voltage decay (OCVD) data of a perovskite solar cell with a TiO_2/MAPi interface. a) Changes in the decay rate appear in the light-soaking stage, b) which slowly revert back during the dark recovery stage. c) An exemplary comparison between three OCVD measurements that show the two photo-induced changes in the decay rate and the buildup of an electrostatic potential, V_{elec} . A–D) The energy diagram at the TiO_2 /perovskite contact at 4 different stages: A) under dark without migrating positive cations and vacancies. B) At a very short illumination time, $\Delta t = 1$ s. C) at an illumination time close to 1 min. D) after a substantial illumination time $\Delta t \gg 1$ min. The band bending results from an increase of hole concentration at the interface, which forms an electrostatic potential, due to the electric field across the interface. This potential is added to the built-in potential. Reproduced with permission^[7] Copyright (2016), Elsevier.

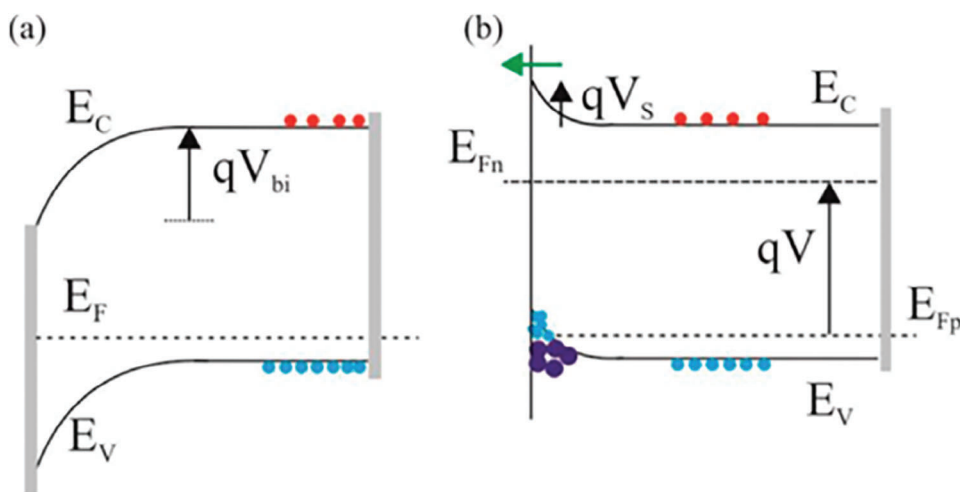


Figure 12. The energy diagram of a perovskite solar cell in which electron selective contact locates at the left and hole selective contact locates at the right side. a) Equilibrium condition in the dark. b) Open circuit under illumination condition. E_C , E_V : Edges of conduction and valence bands. E_F : Fermi Level. E_{Fn} , E_{Fp} : Quasi-Fermi level of electrons and holes. V : External voltage of the contacts. V_{bi} : The constant built-in voltage. V_s : The variable surface polarization voltage. Indicated in (b) are the accumulation of holes and cations, and the tunnelling of electrons across the surface barrier. Reproduced with permission^[116] Copyright 2017, American Chemical Society.

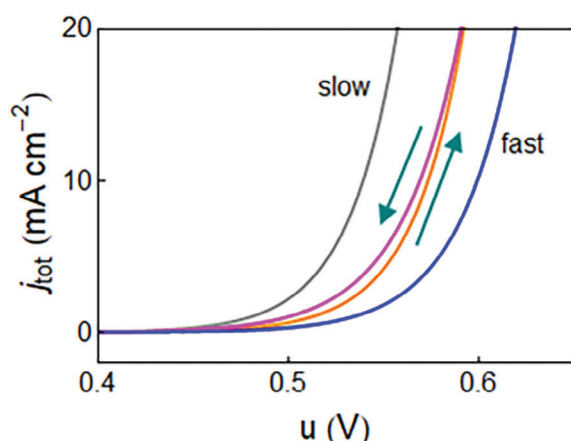


Figure 13. Current–voltage curves for different measurements: stationary (gray), very fast (blue), and constant rate scan cycle. Parameters: $J_{rec0} = 10^{-8}$ mA/cm², $k_B T/q = 0.026$ V, $n_r = 10/9$, $n_s = 10$; $n_{rec} = 1$, $\tau_s = 10$ s, $S_r = 0.05$ V s⁻¹.

We expand the equations to first order, where the perturbation of variable y is indicated as \hat{y} , and the factor functions of each term are computed at equilibrium. Furthermore, we transform the small signal equations to the frequency domain by the Laplace transform, $d/dt \rightarrow s$, where $s = i\omega$ and ω is the angular frequency. We obtain the results^[69]

$$\hat{j}_{tot} = C_m s \hat{u} + g_r \hat{u} + g_s \hat{v}_s \quad (22)$$

$$\hat{v}_s = \frac{\hat{u}}{1 + s\tau_s} \quad (23)$$

The conductances are defined as

$$g_r = \frac{\partial j_{rec}(u, v_s)}{\partial u} = \frac{q}{n_r k_B T} J_{rec}(u) \quad (24)$$

$$g_s = \frac{\partial j_{rec}(u, v_s)}{\partial v_s} = \frac{q}{n_s k_B T} J_{rec}(u) \quad (25)$$

Note that the two conductances have the same voltage dependence and differ only in the prefactor. Using the previous equations, we find the expression of the impedance

$$Z(s) = \frac{\hat{u}}{\hat{j}_{tot}} = \left[C_g s + g_r + \frac{g_s}{1 + s\tau_s} \right]^{-1} \quad (26)$$

Let us define the inductor

$$L_s = \frac{\tau_s}{g_s} \quad (27)$$

The impedance becomes

$$Z(s) = \left[C_g s + g_r + \frac{1}{\frac{1}{g_s} + sL_s} \right]^{-1} \quad (28)$$

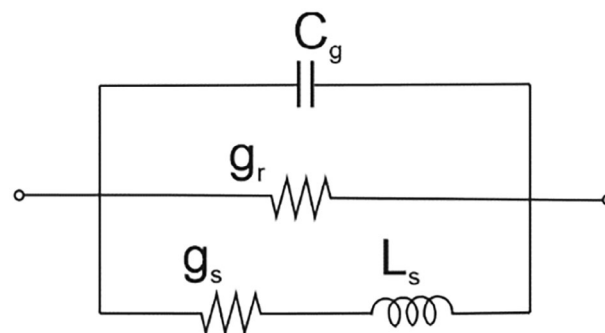


Figure 14. Equivalent circuit model of the chemical inductor.

The impedance model can be represented as the equivalent circuit of **Figure 14**. Characteristic impedance spectra for the parameters of **Figure 13** are shown in **Figure 15**. It is observed that the impedance is first capacitive, as represented by a single positive arc, at low voltage, **Figure 15a**. Then it becomes distorted at low frequency, **Figure 15b**, and finally a full inductive arc is developed, **Figure 15c**, associated to a notorious “negative capacitance” effect.^[94,170–172]

Consider the time constants for the capacitive and for the inductive processes, respectively

$$\tau_a = \frac{C_g}{g_s} \quad (29)$$

$$\tau_s = g_s L_s \quad (30)$$

The calculation of the frequency of intercept of the real axis in **Figure 15c** gives the following result^[69]

$$\omega_c = \left[\frac{1}{\tau_s} \left(\frac{1}{\tau_a} - \frac{1}{\tau_s} \right) \right]^{1/2} \quad (31)$$

Therefore, a crossing of the real axis, is observed only if ω_c is real, when $\tau_s > \tau_a$. The inductive process is established at the frequencies corresponding to the characteristics times at which

$$\tau_s = \tau_a(u) \quad (32)$$

In **Figure 15c** we can observe that the conductance at intermediate frequencies is g_r , and the inductor effect makes the conductance *increase* to the dc conductance at very low frequencies

$$g_{dc} = g_r + g_s \quad (33)$$

In solar cells this process is interpreted as an increase of recombination at the longest times of measurement, governed by ion motion, that is deleterious for the photovoltaic performance.^[29] The quantification of the negative capacitance is therefore important to mitigate ionic diffusion^[21] and the resultant adverse interfacial recombination pathways.^[173]

The impedance patterns of Equation (28) and **Figure 15** emerge from the general structure of Equations (15) and (16) (with the added capacitive term) and produce the general denominator of the chemical inductor,^[69,162] that provides a basic explanation to the widely observed “negative capacitance”.^[94,170–172]

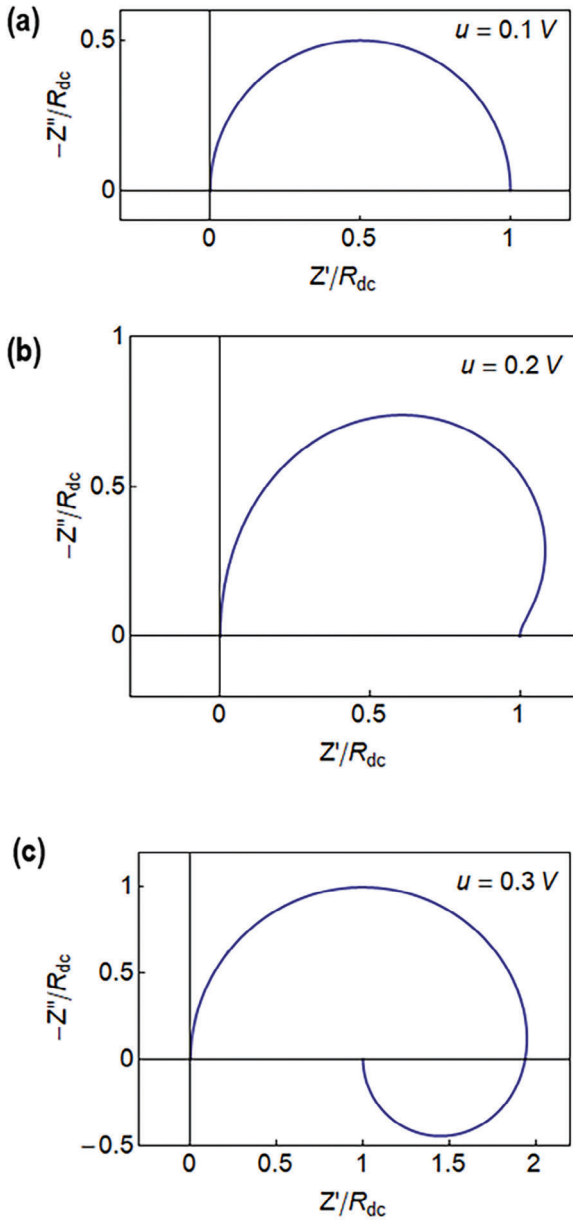


Figure 15. Normalized impedance spectroscopy spectra at different applied voltages, for the parameters of Figure 2 with a capacitor $C_g = 10^{-4} \text{ F cm}^{-2}$.

For example the HH model in Equations (11)–(14) is composed by the parallel combination of three chemical inductors, and this is confirmed by the calculation of the impedance model.^[174] The inductive process causes the increase of current at long times observed in Figure 2, which is the origin of inverted hysteresis in Figure 13, hence we call it inductive hysteresis.^[84]

9. Capacitive Effects

The Figures 6 and 16 show the measurement current–voltage cycles and impedance response of halide perovskite memristors of different compositions. We observe that the properties described

by the slow surface recombination model in Figures 13 and 15 are generally satisfied in the experiments: A large inverted hysteresis occurs in the current–voltage curve, accompanied by the notorious inductive arcs in the impedance spectra. This pattern has also been obtained in single crystal memristors.^[175]

However, there are additional features not described in the simple model. In PSCs there is often not one, but two, and even three, separate capacitive processes at low voltages.^[26,31] This is shown in Figure 17b, in the form of different plateaus of the capacitance–frequency plot. Therefore, more complex models, need to be used and justified.

In fact, based on the physical picture of Figure 12 in the SPM^[116] a more complex neuron-style model was suggested. The recombination rate of electrons depends on the surface accumulated hole charge Q_s as follows:

$$j_{\text{rec}}(u, v_s) = \frac{Q_s(v_s)}{\tau_{\text{rec}}(u)} \quad (34)$$

Here, the recombination lifetime is an exponential function as it includes the dependence of the electron density,^[176,177]

$$\tau_{\text{rec}}(u) = \tau_{\text{rec}0} e^{-\frac{qu}{n_r k_B T}} \quad (35)$$

The $\tau_{\text{rec}0}$ is the prefactor and n_r the ideality factor of the lifetime.

In addition to the recombination current, the surface charge in Figure 12 produces a polarization current.^[116] The model (18–19) is extended as follows:

$$j_{\text{tot}} = C_g \frac{du}{dt} + j_{\text{rec}}(u, v_s) + \frac{dQ_s}{dt} \quad (36)$$

$$\tau_s \frac{dv_s}{dt} = u - v_s \quad (37)$$

The surface charge $Q_s(v_s)$ depends on the surface voltage v_s . The surface capacitance is:

$$C_s(v_s) = \frac{dQ_s}{dv_s} \quad (38)$$

So that the current becomes

$$j = C_s \frac{dv_s}{dt} \quad (39)$$

Experimentally the capacitance observed in the low frequency range depends exponentially on the voltage,^[87,178] thus we write

$$C_s(v_s) = C_{s0} e^{\frac{q}{k_B T} \frac{v_s}{n_s}} \quad (40)$$

By integration of Equation (38) we obtain the expression

$$Q_s(v_s) = \frac{n_s k_B T}{q} C_{s0} e^{\frac{q}{k_B T} \frac{v_s}{n_s}} = \frac{n_s k_B T}{q} C_s(v_s) \quad (41)$$

Combining Equations (35) and (40) we remark that the recombination current can be written again as:

$$j_{\text{rec}}(u, v_s) = J_{\text{rec}0} e^{\frac{q}{k_B T} \left(\frac{u}{n_r} + \frac{v_s}{n_s} \right)} \quad (42)$$

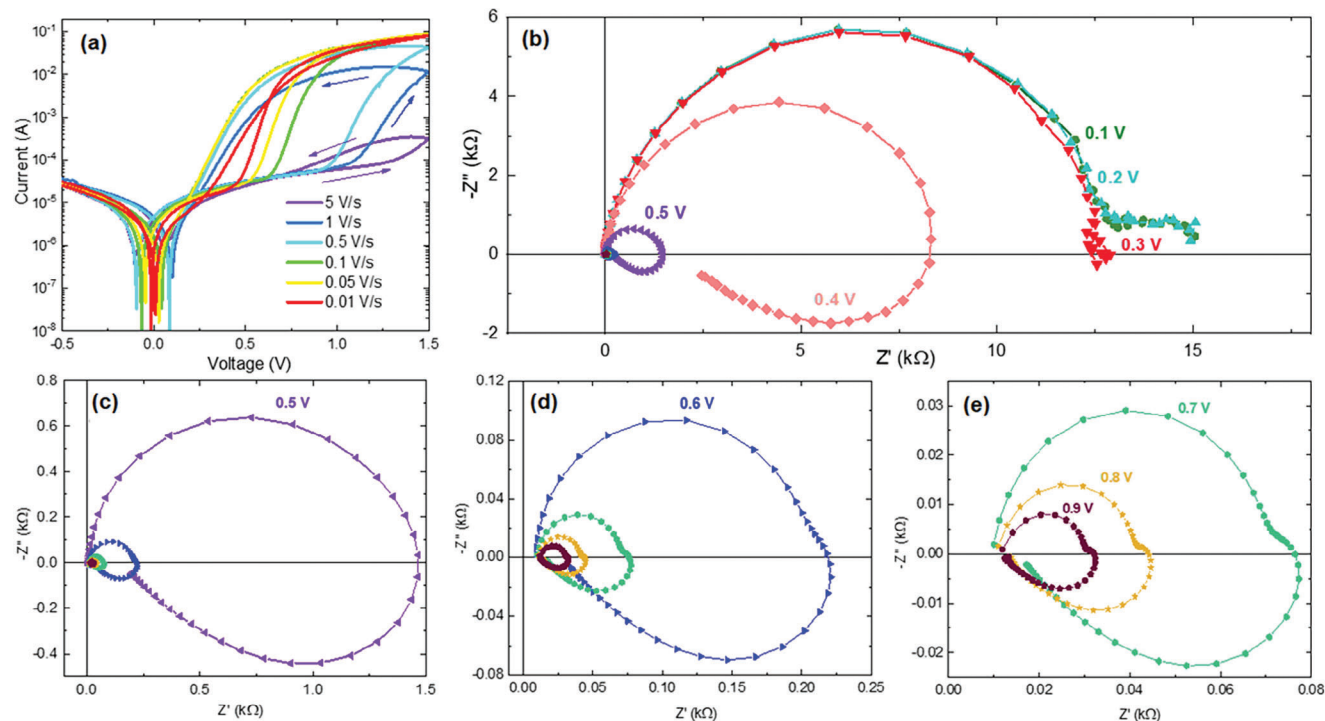


Figure 16. a) Current–voltage characteristic for a FTO/PEDOT:PSS/MAPI/Au memristor device at six different scan rates starting from 5 V s^{-1} . Arrows indicate sweep direction. b,c,d,e) Complex plane plot representation of the impedance spectra at different applied dc voltage. (c), (d), and (e) plots correspond to a magnification of the scales. Reproduced with permission^[78] Copyright 2022, Creative Commons Attribution (CC BY 4.0) license.

where

$$J_{\text{rec}0} = \frac{n_s k_B T C_{s0}}{q \tau_{\text{rec}0}} \quad (43)$$

We calculate the impedance response of the model (36-37). By small perturbation we obtain the equations

$$\hat{J}_{\text{tot}} = C_g s \hat{u} + g_r \hat{u} + g_s \hat{v}_s + C_s s \hat{v}_s \quad (44)$$

$$\hat{v}_s = \frac{\hat{u}}{1 + s\tau_s} \quad (45)$$

Using the previous equations we find the expression of the impedance

$$Z(s) = \frac{\hat{u}}{\hat{J}_{\text{tot}}} = \left[C_g s + g_r + \frac{g_s}{1 + s\tau_s} + \frac{C_s s}{1 + s\tau_s} \right]^{-1} \quad (46)$$

Let us define the additional conductance

$$g_C = \frac{C_s}{\tau_s} \quad (47)$$

The impedance becomes

$$Z(s) = \left[C_g s + g_r + \frac{1}{\frac{1}{g_s} + sL_s} + \frac{1}{\frac{1}{g_C} + \frac{1}{C_s s}} \right]^{-1} \quad (48)$$

The equivalent circuit arising from this model is shown in **Figure 18**.^[116] It adds a capacitive line C to the basic equivalent circuit of the chemical inductor in **Figure 14**, that is formed by the lines ABD. This large low frequency capacitance is an important property of PSCs. The combination C-D is an outcome of the surface polarization model^[31,116] and some memristor models.^[78] Furthermore the model (36-37) has the property that the time constants of the two branches C and D are the same:

$$\tau_{\text{kin}} = \frac{C_s}{g_C} = g_s L_s \quad (49)$$

This is a consequence of the recombination expression (34). This property enables a single kinetic time τ_{kin} to be defined when the system makes a transition between capacitive and inductive hysteresis, discussed in Section 15. The transition occurs near the self crossing of the current–voltage curve, as observed in **Figure 1a**, and remarked in **Figure 6**. The constant kinetic time across the transition predicted by Equation (49) has been observed experimentally.^[68,72]

10. Delayed Current Model

Instead of the slow voltage, the memory effect can be formed with a slow current j_d as a state variable. This is a common resource in simplified neuron models, such as the FitzHugh–Nagumo^[179]

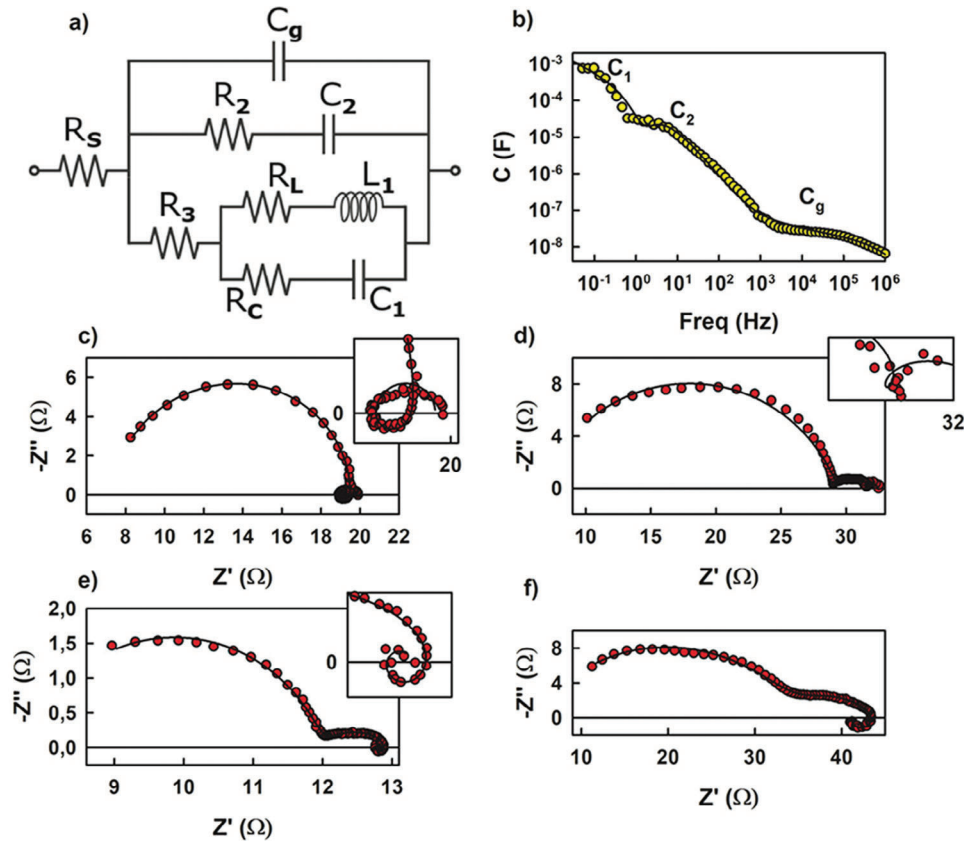


Figure 17. a) Equivalent circuit for the data fitting of IS of carbon-based perovskite solar cells. Three devices with different thickness, named 1, 2, 3, were analyzed. b) Capacitance–frequency plot of Cell 2 showing three capacitances at different frequencies. d–f) Impedance complex plots at open circuit conditions. Red and yellow points are experimental data, and the straight black line is the fitting given by the equivalent circuit. (c) is for Cell 1, (d,e) are for Cell 2, and (f) is for Cell 3. Reproduced with permission^[31] Copyright 2020, Creative Commons Attribution (CC BY 4.0) license.

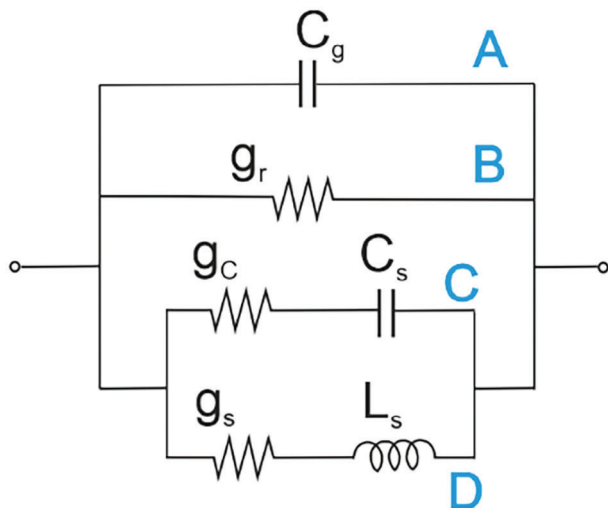


Figure 18. Equivalent circuit of the surface polarization model.

and the exponential adaptive^[180] models. The model is formulated as follows:

$$J_{tot} = \frac{u}{R_b} + j_d + C_g \frac{du}{dt} \quad (50)$$

$$\tau_d \frac{dj_d}{dt} = J_d(u) - j_d \quad (51)$$

The model contains a background ohmic current with resistance R_b . The variable j_d in Equation (50) is an additional parallel current with equilibrium form $J_d(u)$, governed by an equilibration time τ_d .

By small perturbation we obtain the equations

$$\hat{j}_{tot} = \frac{\hat{u}}{R_b} + C_g s \hat{u} + g_r \hat{u} + \hat{j}_d \quad (52)$$

$$\hat{j}_d = \frac{g_d \hat{u}}{1 + s\tau_d} \quad (53)$$

The conductance is defined by

$$g_d = \frac{\partial J_d}{\partial u} = \frac{q}{n_d k_B T} J_d \quad (54)$$

and the inductor is

$$L_d = \frac{\tau_d}{g_d} \quad (55)$$

We find the expression of the impedance

$$Z(s) = \frac{\hat{u}}{\hat{j}_{tot}} = \left[\frac{1}{R_b} + C_g s + \frac{1}{\frac{1}{g_d} + sL_d} \right]^{-1} \quad (56)$$

It is the same as Equation (28) represented in Figure 14.

The impedance forms again the chemical inductor model of Figure 14 with the characteristic responses of Figure 15. The interpretation of the model is shown in Figure 19a,b. The current increase with time is the characteristic effect of the inductor mechanism.

For a solar cell j_d has the equilibrium value^[68]

$$J_d(u) = J_{d0} e^{\frac{qu}{n_d k_B T}} \quad (57)$$

in terms of another ideality factor n_d . For a perovskite photodetector, the slow variable is a photocurrent.^[77]

For perovskite memristors^[74] the form

$$J_d(u) = J_{d0} X(u) \quad (58)$$

is employed, where

$$X(u) = \frac{1}{1 + e^{-q(u - V_T)/V_m}} \quad (59)$$

Similarly to HH variables, the function X is activated from 0 to 1 at the threshold voltage V_T , and V_m describes the steepness of the rise. Hence the slow current component of the memristor rises from 0 to J_{d0} . The results of this model are shown in Figure 19. Figure 19c shows the equilibrium current, that raises up to J_{d0} when $x \rightarrow 1$, and Figure 19d shows the hysteresis effect when the voltage is cycled, due to the delay of j_d . Figure 19e shows time transient response that will be analyzed in Section 14.

11. Drift Electronic Transport and Memory Effects in the Conductance

So far we have described models based on the picture of Figure 4, in which the voltage u controls the charge density, and the current is governed by recombination, since transport is fast and the current direction is determined by the selective contacts. This was justified by nearly flat response of the photocurrent in the region around the short-circuit condition, as shown in Figure 5. When photovoltaic technologies become mature, the photocurrents in the high-efficiency devices nearly match the radiative balance limit. However, it is more difficult to suppress the remainder nonradiative recombination effects that make the V_{oc} lower than the maximum possible value.^[127,182] This general tendency can be readily checked at the AMOLF tables of champion devices (<https://www.lmpv.nl/db/>). In the case of perovskite solar cells, the minor voltage dependence of the photocurrent is due to the fact that diffusion lengths are very long^[183] compared to other technologies with smaller carriers mobilities.^[184] The slow current models described in Section 10 still correspond to recombination models, in which the delayed current is associated to a secondary recombination process.

Nevertheless, charge collection processes by a drift field has a dominant contribution to the current response in many devices. One example is shown in the perovskite photodetector of Figure 20, where the contacts are symmetric and the photocurrent is fully dependent of the applied electrical field.^[181] Nearly ohmic ohmic current–voltage characteristic can be observed with the slope increasing by the photogeneration rate. In this case one can assume that the voltage operation creates tilted bands representing the constant electrical field that causes drift transport, as indicated in Figure 21. These basic considerations are explained in detail in my book.^[127] The intrinsic built-in voltage V_{bi} is due to the initial difference of work functions of the contacts.

As mentioned earlier many models of hysteresis of PSC rely on charge collection issues according to the ionic polarization between the contacts, especially for inverted hysteresis.^[79,135,169,185–187] The hysteresis properties in these models, stem from the significant disproportion in the movement speeds of ions compared to electrons/holes, along with their sufficiently high concentration to efficiently shield the external potential (comprising built-in and applied potential) over extended durations, but only partially during shorter intervals. The picture of the drift field influenced by ions is shown in Figure 22^[185] and detailed simulations are shown in Figure 23.^[186] This picture can provide large disparity of currents near SC point, as in early PSC devices that had charge collection issues, see Figure 24d.^[135] This “ion induced field screening”^[188] is useful when the photocurrent is severely affected, as in degradation. In the high-performance solar cells, though, the hysteresis is dominated by recombination close to V_{oc} , as commented before.

Let us review the neuron-style models where carrier drift transport is a dominant characteristics. We remark that the drift transport model with memory effect is already found in the HH models Equation (11). For example in $g_{Na} m^3 h (u - E_{Na})$, the E_{Na} has the role of a built-in voltage, and the transport is fully ohmic. The conductance g_{Na} is a constant, and the passage of current is governed by variables m , h that indicate if the conduction channel is open or closed.

In general the functional dependence of a rectifying ion channel^[189–194] with equilibrium voltage E_c is:

$$I_{tot} = g_0 x (u - E_c) \quad (60)$$

$$\tau_k \frac{dx}{dt} = X(u) - x \quad (61)$$

The term $(u - E_c)$ represent the drift electrical field, and the state variable x corresponds to voltage-gated processes typical of activation and inactivation in pore gates.^[195] The open conductance probability given by Equation (59) corresponds to the Boltzmann open channel probability^[191] that indicates the fraction of conducting sites according to the applied voltage of electrical field.

Let us consider a related approach in the memristor model developed by Miranda and coworkers.^[196–198]

$$I_{tot} = [g_L + (g_H - g_L) x] u \quad (62)$$

$$\frac{dx}{dt} = \frac{(1-x)}{\tau_s(u)} - \frac{x}{\tau_r(u)} \quad (63)$$

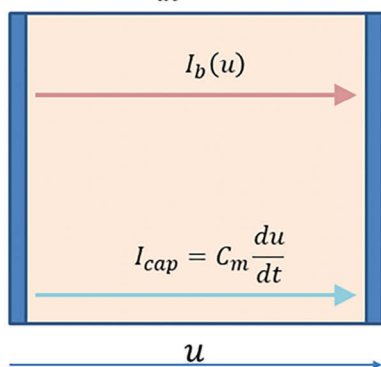
Chemical inductor

$$I = C_m \frac{du}{dt} + I_b(u)$$

$$\tau_k \frac{dI_b}{dt} = I_b^{eq}(u) - I_b$$

(a) Short time response

$$I = C_m \frac{du}{dt} + I_b(u)$$



(b) Long time response

$$I = I_b(u) + I_d(u)$$

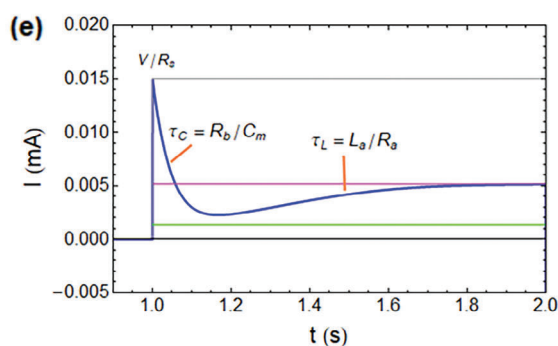
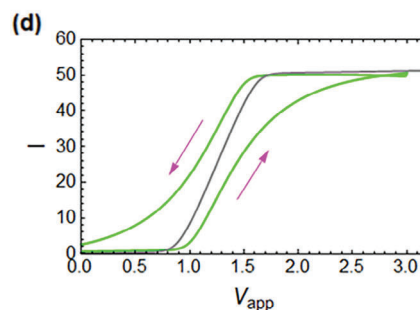
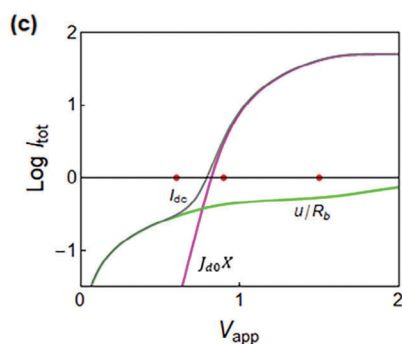
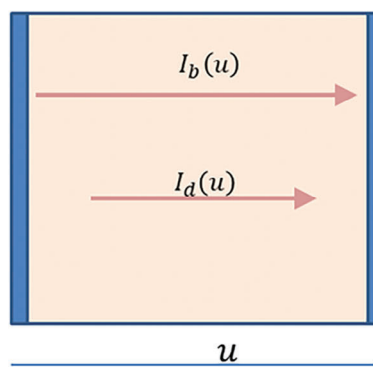


Figure 19. a,b) Dynamical operation of a chemical inductor model composed of a capacitive current $C_m du/dt$, an instantaneous current I_b , and a delayed current I_d . Under a step of the voltage u the capacitive current decreases since the first moment, and the current increases from the instantaneous value I_b to the final value $I_b + I_d^{eq}$, after a time τ_k . c) Logarithmic current–voltage curve for the model memristor, showing the two component currents and the total equilibrium dc current (gray line). d) The grey line is the equilibrium current–voltage curve, and the green lines are the current when the external voltage is cycled at a constant scan rate $S_r = 0.05$. Parameters $R_s = 0.01$, $R_b = 2$, $C_m = 10$, $\tau_k = 10$, $J_{d0} = 50$, $V_T = 1$, $V_m = 0.05$. e) Transient charging current for the memristor model for a square voltage pulse $V_{app} = 1.5$. Parameters $R_b = 10^3$, $R_s = 100$, $C_m = 10^{-3}$, $J_{d0} = 10^{-2}$, $V_T = 1$, $V_m = 0.05$; $\tau_k = 1$; $\tau_s = 0.1$. Grey line is $\Delta I = V_{app}/R_s$, magenta line is V_{app}/R_{dc} , green line is $V_{app}/(R_s + R_b)$. The characteristic times of the decay features are indicated. c–e) Reproduced with permission^[74] Copyright 2023, Creative Commons Attribution (CC BY 4.0) license.

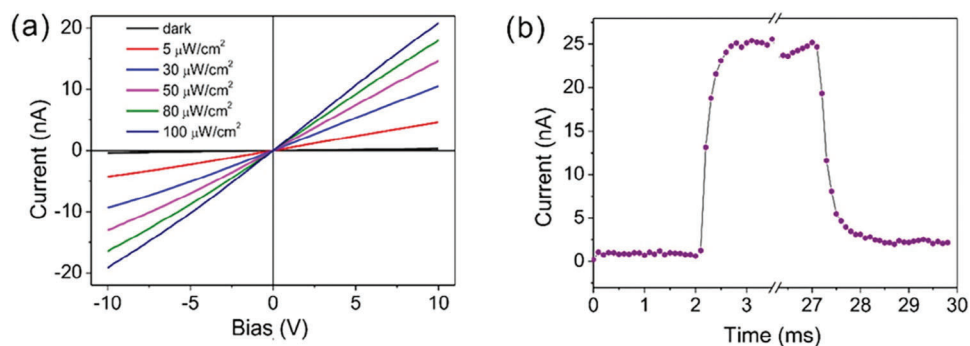


Figure 20. a) I - V curves of a MAPI perovskite photodetector under different illumination power densities at a bias voltage of 10 V. b) I - t curve illuminated by 650 nm light ($100 \mu\text{W cm}^{-2}$) at a bias voltage of 10 V. The time interval was 0.1 ms. Reproduced with permission^[181] Copyright 2015, American Chemical Society.

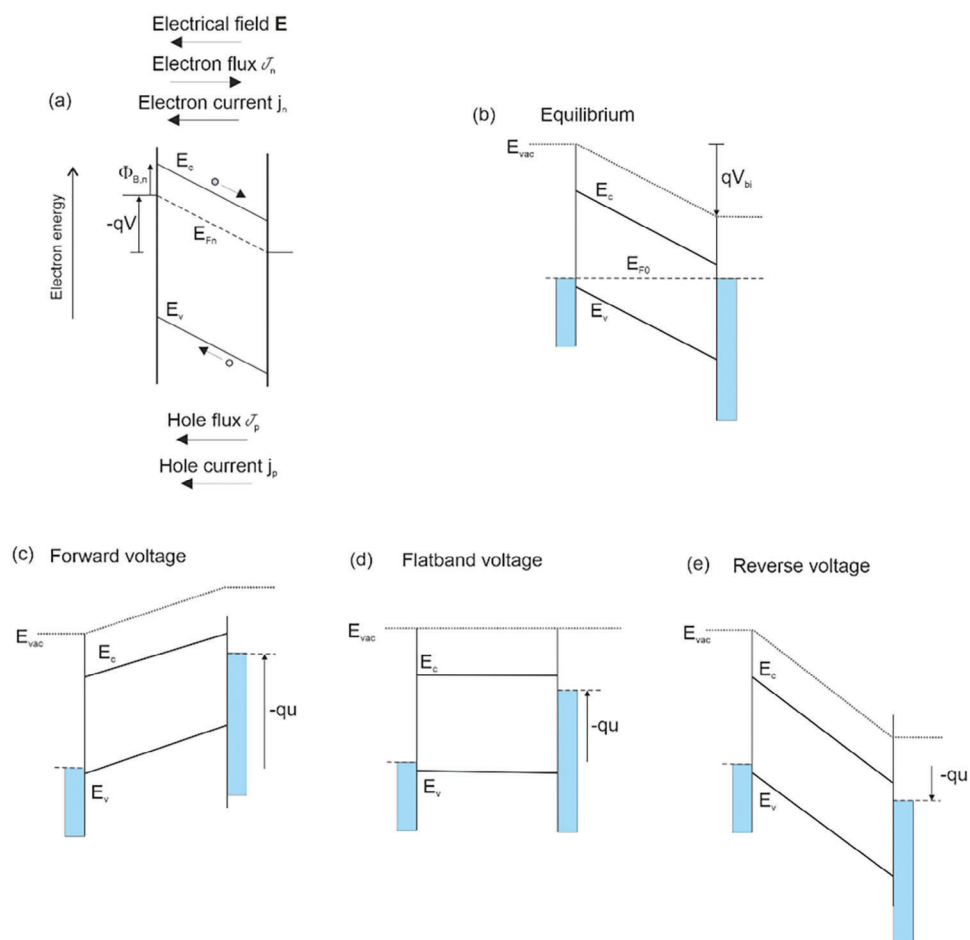


Figure 21. a) Energy diagram of an electron conducting layer material with applied bias potential. q is the elementary charge, u is the voltage applied at the left terminal, E_c is the energy of the conduction band, E_v is the energy of the valence band and E_{Fn} is the Fermi level. All labeled quantities are represented with respect to electron energy scale shown at the left side and local potentials in the semiconductor are represented with respect to a separate scale shown at the right side. The arrows on top and in the bottom show the vector direction of the indicated magnitudes. b-e) Energy diagram of an insulator layer that is contacted by two metals of dissimilar work function, under different cases of applied voltage as indicated.

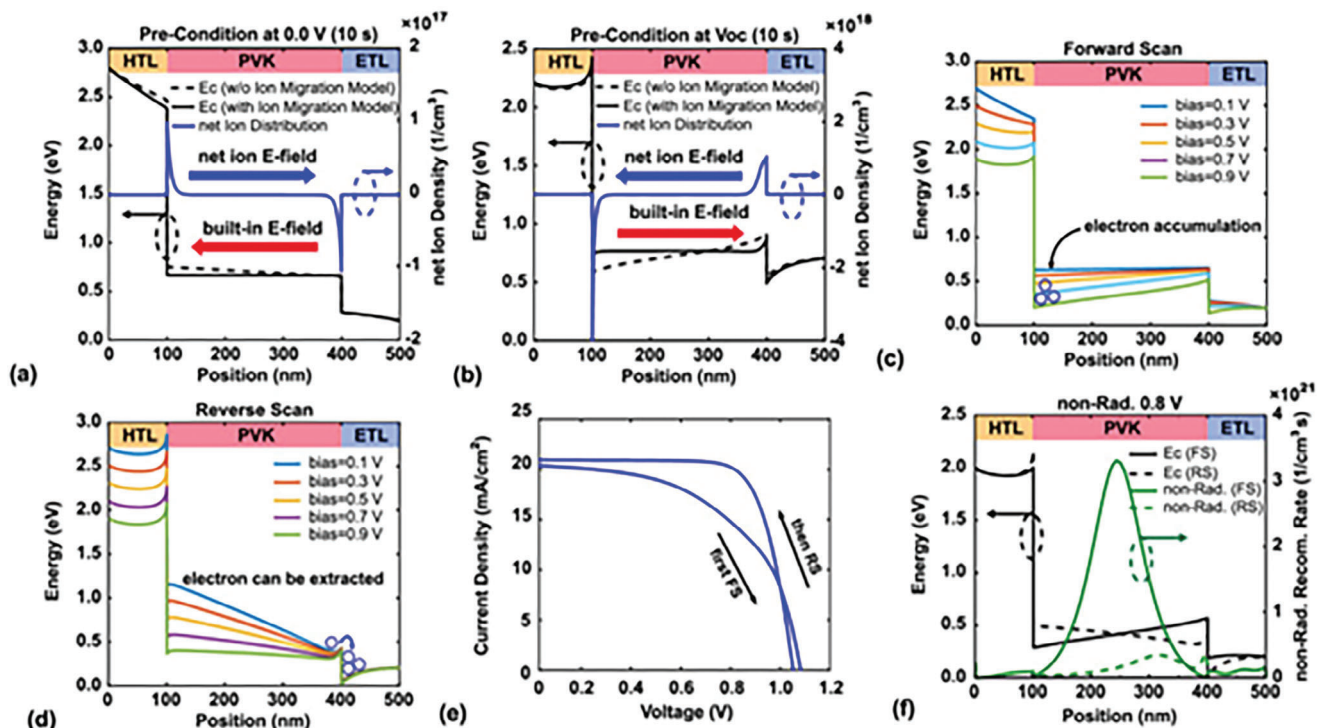


Figure 22. Hysteresis by ion polarization at the contacts in PSC. a,b) are band diagram and net ion distribution for preconditioning at 0 V and V_{oc} , respectively. c,d) Changes in the band diagram when bias is applied under forward and reverse scanning conditions, respectively. e) J - V characteristics under forward and reverse scanning conditions. f) Band diagram and non-radiative recombination rate under forward and reverse scanning conditions at a bias of 0.8 V. Reproduced with permission^[185] Copyright 2022, Creative Commons Attribution (CC BY 4.0) license.

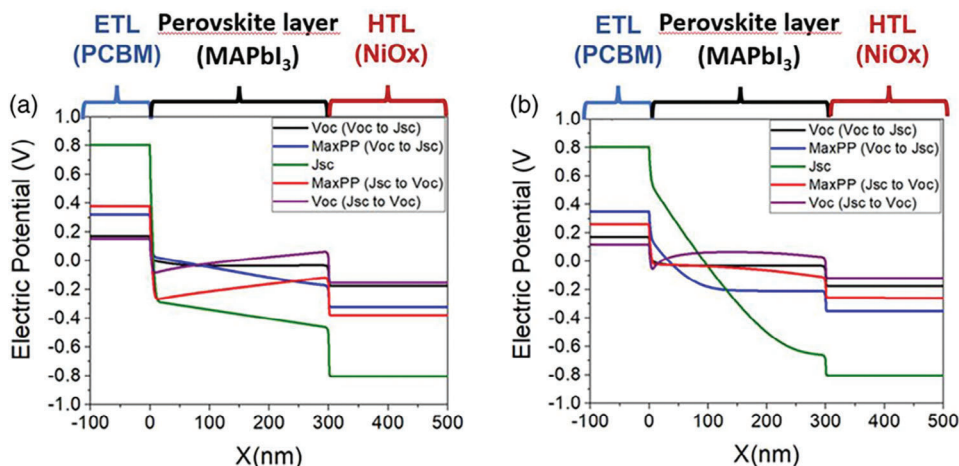


Figure 23. Snapshots of electric potential versus distance from ETL (electron transport layer)/perovskite interface x (nm) for the p-i-n architecture, where $x = 0$ represents the ETL/perovskite interface and $x = 300$ the perovskite/HTL (hole transport layer) interface. The left panel (a) shows the results at the scan rate for maximum normal hysteresis, and the right panel (b) shows the scan rate for maximum inverted hysteresis $V_{app} = V_{oc}$ (black at start of reverse scan, purple at end of forward scan). In both panels several positions in the J - V curve are shown: $V_{app} = V_{mpp}$ (reached during reverse (blue), forward (red) scan), $V_{app} = 0$ (green). In all simulations a 40 s preconditioning bias of 1.2 V has been applied. It must be noted that longer preconditioning times led to faster convergence in the numerical result. Reproduced with permission^[186] Copyright 2022, Creative Commons Attribution (CC BY 4.0) license.

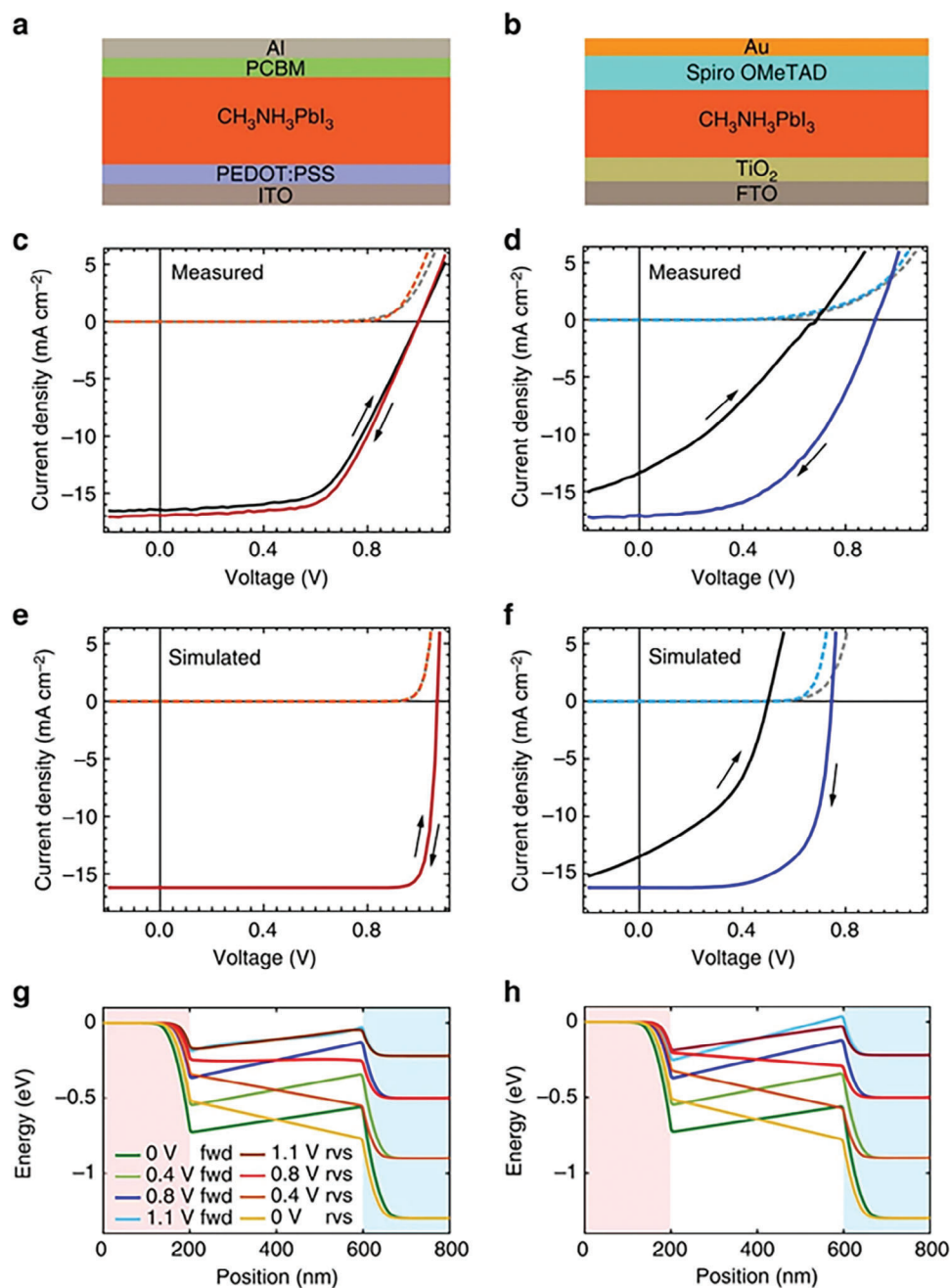


Figure 24. a) Top cathode and b) bottom cathode perovskite solar cell device architecture stacks. Measured current–voltage curves in the dark and under 1 sun equivalent illumination scanned at $\approx 40 \text{ mV s}^{-1}$ in the forward (reverse-to-forward bias) and reverse (forward-to-reverse bias) directions for the c) top cathode cell, which showed a reverse scan (red curve) power conversion efficiency of 9.3% and a hysteresis index (HI) of 0.05, and d) the bottom cathode cell, which showed a reverse scan (blue curve) power conversion efficiency of 7.7% and HI = 1.71. Dashed orange and light blue curves show the forward dark scan for top and bottom cathode devices, respectively. Black curves show the forward 1 sun scans, while dashed grey curves show the reverse dark scan for top and bottom cathode devices, respectively. The corresponding simulated current–voltage scans in each scan direction are shown for a p-i-n device structure with mobile ions, without (e) and with (f) recombination in the p- and n-type contact regions. The simulated values of HI were 0.00 and 1.84, respectively. The simulated scan protocol was similar to the experimental measurement at 40 mV s^{-1} . Simulated electrostatic potential profiles during forward (fwd) and reverse (rvs) J–V scans for the g) top cathode and h) bottom cathode device. The p- and n-type layers are indicated by pink and blue shaded regions, respectively. Reproduced with permission^[135] Copyright 2016, Creative Commons Attribution (CC BY 4.0) license.

$$\tau_s = \tau_0 e^{-\frac{u-V_s}{n_s V_m}} \quad (64)$$

$$\tau_r = \tau_0 e^{\frac{u-V_r}{n_r V_m}} \quad (65)$$

In this model, the variable $0 \leq x \leq 1$ modulates the conductance between the low g_L and high conductance g_H states of the memristor. The relaxation times for SET, τ_s , and RESET, τ_r , processes, produce again the sigmoidal form (59) in equilibrium. The exponential dependence of the relaxation times introduces additional properties for the volatile behavior.

In general the functional dependence of the relaxation times produce significant features in the dynamics of memristors and chemical inductors.^[199] The relaxation times in HH model are strong functions of the voltage, that govern the speed of the transitions. This is important for applications in neuromorphic systems and spiking neurons.^[67,145] However in the PSC model we use a simple approach in which the memory variables show a constant relaxation time. This is supported by experiments, as discussed later. In perovskite memristors for neuromorphic applications it is important to adjust the volatile and nonvolatile characteristics.^[62,200]

In the models of the type (11-14), (60-61), and (62-63) we can separate the effects of the drift field $(u - E_c)/L$ and a generalized conductance G

$$I_{tot} = G(x, u) (u - E_c) \quad (66)$$

$$\tau_k \frac{dx}{dt} = X(u) - x \quad (67)$$

The generalized conductance itself $G = I/V$ is a measurable quantity but usually not a suitable state variable, since it is influenced by physical variables as mobility, and/or state variables for voltage-gated processes typical of activation and inactivation in pore gates.^[140,195] Note that the g_i parameters obtained in our model as in Equation (24) are *differential* conductances that are well defined.

In line with Equation (66) another interpretation of Equations (60) and (61) is suitable, in which $x(u - E_c)/L$ can be viewed as the effective electrical field with a memory effect modulated by the variable x , associated to ionic polarization.^[83] This is the approach of the “ion induced field screening” reviewed above.

Halide perovskite and organic photodetectors display rich phototransient dynamics that are significant for the detection time.^[77,99] This is observed in Figure 20b.^[181] The neuron-style models where the memory variable affects the drift photoconductance conductance have been formulated.^[77] In the model of a perovskite LED the $G(x, u)$ expression combines the exponential recombination current with a gating variable that causes the onset of light emission.^[81]

12. Ionic Transport Effects

A common explanation of memory effects in PSCs is the ionic reorganization produces an electronic effect, in terms of charge collection, or trapping, that enhances the electronic current.^[28,29,116] This mechanism is often suggested for the inverted hysteresis observed in perovskite devices.^[79,94,112,201] In general obtaining

a specific mechanism in the presence of mixed ionic and electronic diffusion in a two-contact device is not straightforward. However, unambiguous effects of ion drift or diffusion have been reported.^[202–204]

For the incorporation of the ion conduction in neuron-style model we can use the following equations:

$$j_{tot} = \frac{dQ_{ion}}{dt} \quad (68)$$

$$\tau_{ion} \frac{dv_{ion}}{dt} = u - v_{ion} \quad (69)$$

Here we introduce the surface ionic charge Q_{ion} and the ionic surface polarization potential v_{ion} , with the relaxation time τ_{ion} in Equation (69). We define the ionic capacitance:

$$C_{ion} (v_{ion}) = \frac{dQ_{ion}}{dv_{ion}} \quad (70)$$

The C_{ion} is associated to the ionic polarization at the interface.^[75,79,205] This last capacitance usually takes intermediate values between the geometric capacitance C_g and the huge low frequency capacitance C_s .^[31] The variable v_{ion} is not associated to a chemical inductor, as it does not participate in the dc conduction current, which is necessarily electronic in the presence of ion-blocking contacts.

13. Perovskite Neuron-Style Models

Different versions of neuron-style models for perovskite devices have been proposed in previous work.^[35,68,71–81] By combining the different approaches outlined in the preceding sections, we can formulate the following general model:

$$j_{tot} = C_g \frac{du}{dt} + j_{rec}(u, v_s) + j_d + \frac{dQ_s}{dt} + \frac{dQ_{ion}}{dt} \quad (71)$$

$$\tau_s \frac{dv_s}{dt} = u - v_s \quad (72)$$

$$\tau_d \frac{dj_d}{dt} = j_d (u) - j_d \quad (73)$$

$$\tau_{ion} \frac{dv_{ion}}{dt} = u - v_{ion} \quad (74)$$

The backbone of the model is composed by one conduction Equation (71) and several delayed memory variables, with the associated relaxation Equations (72)–(74).

The calculation of the impedance spectroscopy response of the neuron-style models has been explained in several publications.^[67,70,72,162,166] We take as reference the general model (71-73). By small perturbation, we obtain the equations:

$$\hat{j}_{tot} = C_g s \hat{u} + g_r \hat{u} + g_s \hat{v}_s + \hat{j}_d + C_s s \hat{v}_s + C_{ion} s \hat{v}_{ion} \quad (75)$$

$$\hat{v}_s = \frac{\hat{u}}{1 + s\tau_s} \quad (76)$$

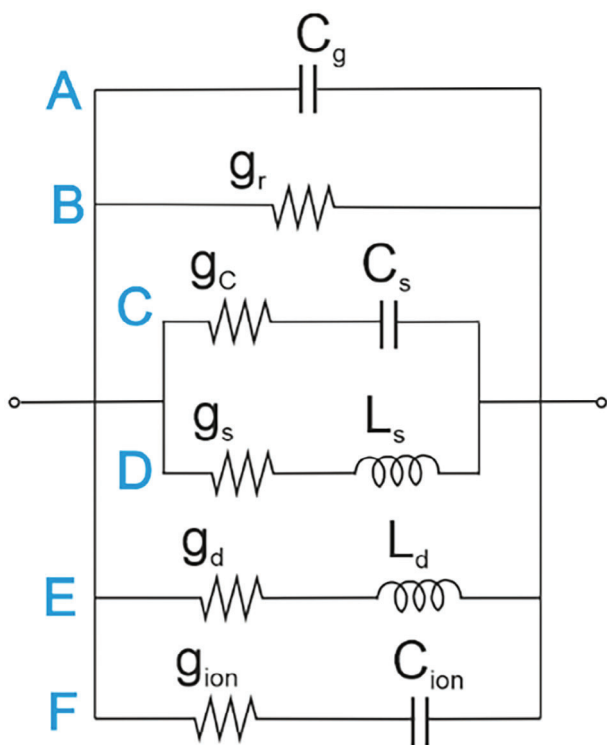


Figure 25. Equivalent circuit model.

$$\hat{j}_d = \frac{g_d \hat{u}}{1 + s\tau_d} \quad (77)$$

$$\hat{v}_{ion} = \frac{\hat{u}}{1 + s\tau_{ion}} \quad (78)$$

Using the previous equations we find the expression of the impedance

$$Z(s) = \frac{\hat{u}}{\hat{j}_{tot}} = \left[C_g s + g_r + \frac{g_s}{1 + s\tau_s} + \frac{g_d}{1 + s\tau_d} + \frac{C_s s}{1 + s\tau_s} + \frac{C_{ion} s}{1 + s\tau_{ion}} \right]^{-1} \quad (79)$$

Using inductor and capacitor elements the impedance becomes

$$Z(s) = \left[C_g s + g_r + \frac{1}{\frac{1}{g_s} + sL_s} + \frac{1}{\frac{1}{g_d} + sL_d} + \frac{1}{\frac{1}{g_c} + \frac{1}{C_s s}} + \frac{1}{\frac{1}{g_{ion}} + \frac{1}{C_{ion} s}} \right]^{-1} \quad (80)$$

The model of Equation (80) is represented as an equivalent circuit in Figure 25. The lines A-D have been already explained in Figure 18. D is the inductor branch of the variable v_s also appearing in Figure 14, but here it is accompanied by a polarization line C, due to the term dQ_c/dt . The line E is the chemical inductor associated to the current variable j_d of Section 10. Thus D and E are somewhat redundant, as they have a similar function, however sometimes several slow current channels in parallel may be required. The line F is the ionic displacement and polarization outlined in Section 12.

The lines C and F correspond to an intermediate frequency relaxation, as they do not allow the passage of current. Both lines

are useful if there are three capacitive processes observed, as mentioned previously.^[26,31]

The application of the model of Figure 25 with the needed components can lead to describe complex spectra with looping features as those shown in Figure 17.^[26,31,206] Furthermore, one can establish additional series connections of elements associated to internal voltage differences, if required. The rationale for Figure 17a is that the R_3 is a bulk recombination in series with the surface recombination resistance R_L . The neuron-style models with series combinations of resistors are described in refs. [68,71]. The application of impedance models to experimental data of perovskite devices is a complex topic and we refer the reader to recent surveys.^[87–91]

14. Time Transient Response

The time domain response of perovskite devices to a voltage or light stimulus forms an important topic with many practical implications, such as the control of hysteresis to measure solar cell performance,^[37,72] the operation of neuromorphic elements,^[74,207] and the kinetic response of photodetectors.^[77] The different capacitive and inductive processes become coupled and provide convoluted features as the voltage is scanned. These properties have been recently described by E. H. Balaguera et al.^[35,72,166,206,208,209] Here we provide a basic introduction to the relevant methods and results.

In order to obtain the basic kinetic behavior we take again the model of Equations (36)–(38), with the slow voltage variable v_s that has equilibrium value $v_s \rightarrow u$.

$$j_{tot} = j_{rec}(u, v_s) + C_s \frac{dv_s}{dt} \quad (81)$$

$$\tau_s \frac{dv_s}{dt} = u - v_s \quad (82)$$

To clarify the physical interpretation of the transient response we apply a small perturbation of the applied voltage at $t = t_0$

$$u = u_0 + \Delta V \quad (83)$$

so that the internal v_s changes with time as

$$v_s = u_0 + \Delta v_s \quad (84)$$

where $\Delta v_s \rightarrow \Delta V$ at long times.

From Equation (20) we have that the recombination current is

$$j_{rec} = J_{rec}(u) - g_s(u) (\Delta v_s - \Delta V) \quad (85)$$

in terms of the conductance g_s . By Equation (82)

$$\frac{dv_s}{dt} = \frac{1}{\tau_s} (\Delta V - \Delta v_s) \quad (86)$$

Using the conductance g_c Equation (81) becomes

$$j_{tot} = J_{rec}(u) + (g_c - g_s) (\Delta V - \Delta v_s) \quad (87)$$

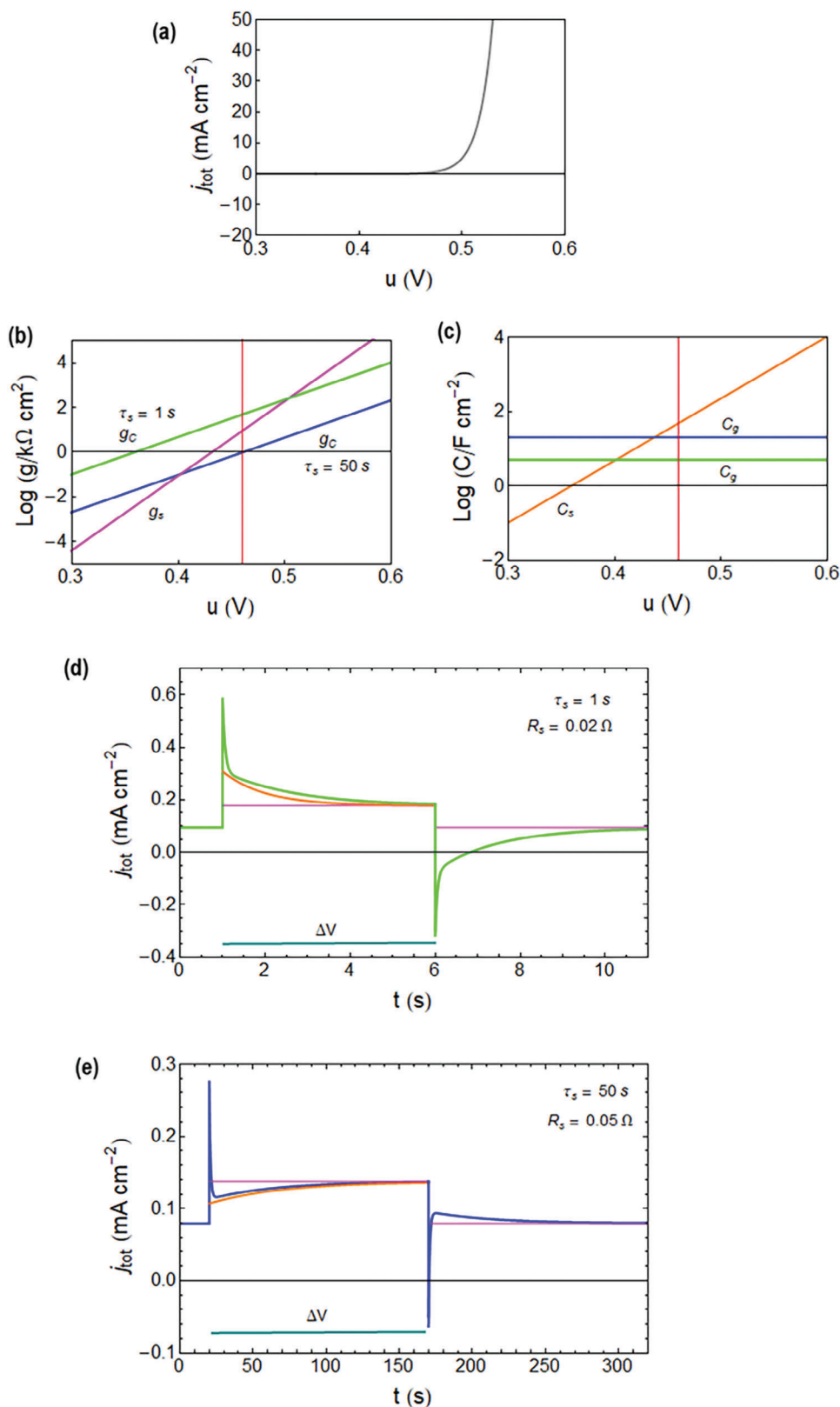


Figure 26. Transient behavior of a model PSC for two cases of τ_s . a) Current–voltage curve. b) Conductances. c) Capacitances. d,e) Transient currents by a square voltage pulse $\Delta V = 0.01$ V at $V_0 = 0.45$ V of duration $\Delta t = 3 \tau_s$. The purple line is the equilibrium current at each voltage, and the orange curve is the linear approximation. Parameters: $k_B T/q = 0.026$ V, $n_r = 1$, $n_s = 1$; $n_r = 0.5$, $J_{\text{rec}0} = 10^{-21}$ mA cm $^{-2}$, $C_0 = 10^{-8}$ F cm $^{-2}$.

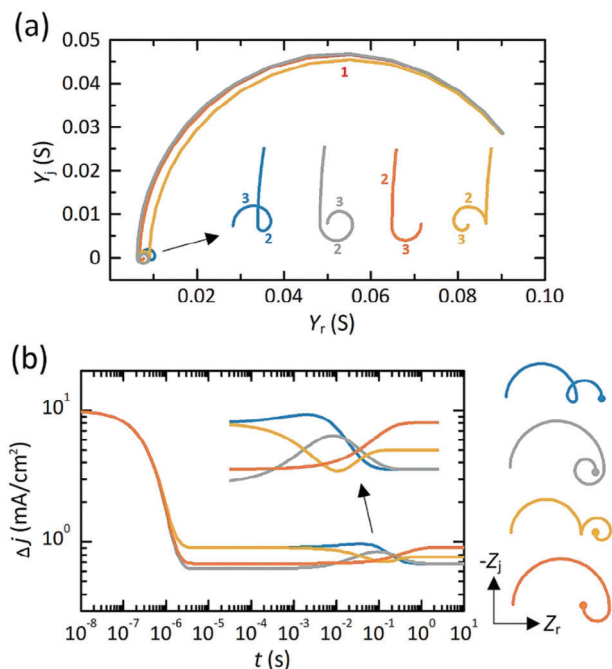


Figure 27. a) Numerical simulations of typical complex plane admittance plots in all types of perovskite semiconductors (e.g., solar cells, photodetectors, light-emitting diodes, and memristors) obtained for different kinetic relaxation constants and applied voltage biases for the impedance patterns consisting of the inductive loop at intermediate frequencies, the spiral, the ideal chemical inductor structure, or the double capacitive arc that finalizes with inductive traces, respectively. Note that the processes have been numbered according to the order of appearance. b) Equivalent current transients in response to a voltage step of 10 mV exhibit a wide variety of dynamics with decays (capacitances), rises (inductors), and spike components. Reproduced with permission^[206] Copyright 2023.

Integrating Equation (86) we find

$$\Delta V - \Delta v_s = \Delta V e^{-t/\tau_s} \quad (88)$$

The time domain response is

$$j_{tot} = J_{rec}(u) + (g_c - g_s) \Delta V e^{-t/\tau_s} \quad (89)$$

In Figure 26 we show the transient response of the current for two different values of τ_s . The change of τ_s causes a variation of the conductance g_c , Figure 26b, so that the sign of $(g_c - g_s)$ is interchanged. In the capacitive domain of voltage where $g_c > g_s$, Equation (89) produces a typical capacitive decay. This is shown in the orange line of Figure 26d. Contrarily, in the inductive domain $g_s > g_c$ there is a current rise from the initial value. This behavior is shown in the orange line of Figure 26e.

The method for the characterization of the small perturbation transients can be generalized to more complex equivalent circuits according to the complexity of the device. In Figure 27 a complete classification of capacitive-inductive-capacitive responses corresponding to the model (90-92) is presented.^[206]

In order to obtain a more general kinetic behavior, we can use the Equations (81-82) for an arbitrary large perturbation ΔV . In practical terms it is important to consider the effect of the series resistance R_s as mentioned in Equation (17), and the geomet-

ric capacitance C_g that is present in most devices. The extended equations become:

$$V = R_s j_{tot} + u \quad (90)$$

$$j_{tot} = j_{rec}(u, v_s) + C_s \frac{dv_s}{dt} + C_g \frac{du}{dt} \quad (91)$$

$$\tau_s \frac{dv_s}{dt} = u - v_s \quad (92)$$

These equations are solved numerically in Figure 26d,e (green and blue lines). We observe an initial spike due to the initial voltage in the series resistance, and the charging of the geometric capacitance in the time $R_s C_g$. Then appear either the capacitive charging of the surface capacitance, Figure 26d, or the response of the inductor, Figure 26e. Upon disconnection, the peak is inverted. These forms are quite general provided that the capacitive and inductive elements are included in the model, as shown in Figure 19e. Further details of the transients are explained in ref. [74].

Based on these insights we can understand a number of important experimental features. First we obtain an explanation of the time transients reported in the literature. In the capacitive domain of voltage where $g_c > g_s$, there is a typical capacitive decay shown experimentally in the points b, c of Figure 1. As shown in Figure 3, the capacitive transient time depends on the voltage value.^[37] Contrarily, in the inductive domain $g_s > g_c$ there is a current rise from the initial value, as shown in Figure 1d, e. After the initial peak due to the high frequency capacitance of the solar cell, the current increases due to the effect of the chemical inductor.^[35,94,206]

The current response described in Figure 26 is an important resource for understanding the response of a perovskite memristor to a train of voltage pulses as shown in Figures 8 and 9. An additional property is shown in these figures: the system remembers the final conductance at the end of each pulse, and the conductance grows progressively. This is the essential functionality for establishing multistate synapses in neuromorphic computation.^[57,61,210-215] Figure 28b shows the potentiation behavior corresponding to the voltage points indicated in the current-voltage curve of Figure 28a.^[73] The individual transients in Figure 28d display an initial capacitive peak and a rise of the current along the voltage square. The system remembers the stored current from one step to the next one, which produces a growth of the current. We conclude that the chemical inductor is an essential feature for the gradual rise of the synaptic conductivity.^[216,217] As shown recently, the connection between the evolution of conductance and the inductive property can be investigated by impedance spectroscopy, tracking the dominant impedance components at low frequency while recording the evolution of resistance/conductance in pulsed or continuous mode.^[74,207,218]

15. The transition of Hysteresis from Capacitive to Inductive

The response of small transients to successive voltage steps is a fundamental resource for understanding the properties of hysteresis in current-voltage curves, as already discussed in Figure 3.

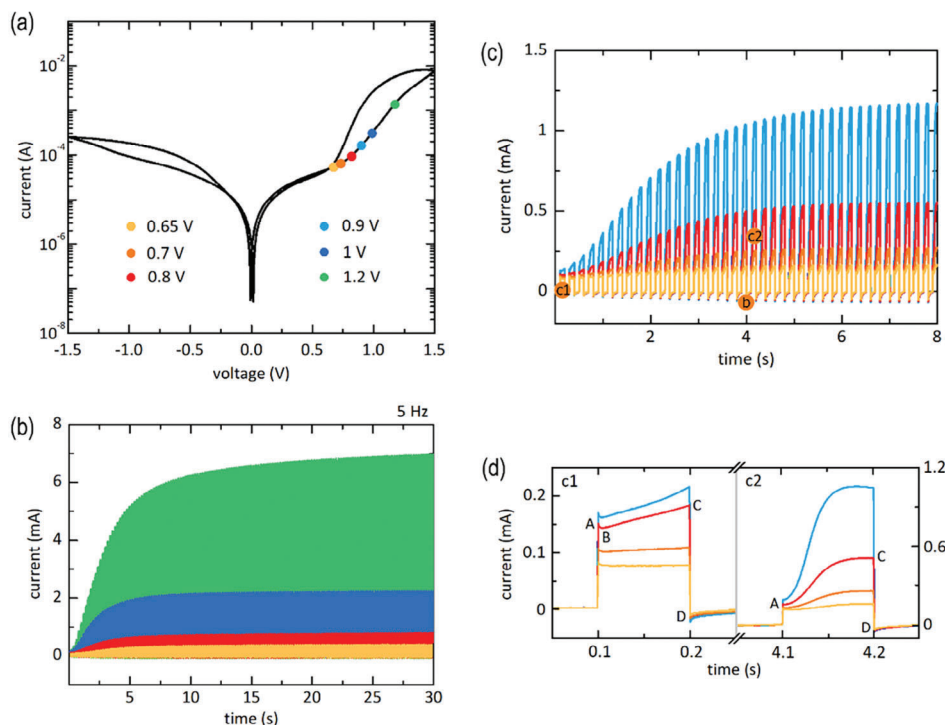


Figure 28. a) Current–voltage response of a perovskite halide memristor measured at a scan rate value of 100 mV s^{-1} , with consecutively increased voltage steps (5 mV) that induce gradual setting and resetting mechanisms. b) Transient currents in response to a train of rectangular pulses of some of the indicated voltage in (a) –from 0.65 to 1.2 V– and 5 Hz, demonstrating the long-term potentiation of the device’s conductance. c) Waveforms of the resulting currents in response to the initial part of the voltage pulse-train stimulus. For the sake of clarity, only time transients to the lower voltage excitations are shown here. d) Representative transition from classical negative transient spikes (c1), found in the initial part of the current response, to progressively enhanced inductive dynamics (c2), as an example of the artificial synaptic potentiation, obtained under the application of numerous voltage pulses. Reproduced with permission^[73] Copyright 2023, Creative Commons Attribution (CC BY 4.0) license.

The interpretation of capacitive hysteresis is shown in **Figure 29**, and the rationale for inductive hysteresis is shown in **Figure 30**, as explained in detail elsewhere.^[84]

One example for PSC was shown in **Figure 1**.^[72] We see a self-crossing of the current–voltage curve at $\approx 1 \text{ V}$, associated to a change of the hysteresis type, as also observed in **Figures 6** and **9**. Let us discuss the application of neuron-style models to account for these features.

We assume again a small perturbation approach for slight hysteresis. The memory variable remains close to its equilibrium value, hence:

$$v_s = u - \Delta v_s \quad (93)$$

We thus have from **Equation (82)**

$$\frac{d\Delta v_s}{dt} = \frac{du}{dt} - \frac{\Delta v_s}{\tau_s} \quad (94)$$

Under the dynamic sweep of **Equation (1)**,

$$\frac{d\Delta v_s}{dt} = S_r - \frac{\Delta v_s}{\tau_s} \quad (95)$$

Therefore

$$\Delta v_s = S_r \tau_s (1 - e^{-u/S_r \tau_s}) \quad (96)$$

Equation (81) becomes

$$j_{\text{tot}} = J_{\text{rec}}(u) + (g_C - g_s) S_r \tau_s (1 - e^{-u/S_r \tau_s}) \quad (97)$$

For a forward voltage scan $S_r > 0$ in **Equation (1)**. Then the sign of the excess hysteresis current in **Equation (97)** depends on the dominant conductance. If $g_C > g_s$ the forward current is positive, corresponding to capacitive hysteresis. If, conversely, $g_C < g_s$, then the forward current is negative, and the hysteresis is inverted, or inductive.^[84] Complete integration methods of the dynamical equations are presented in ref. **[71]**.

The result **(98)** is obtained for a small perturbation, which allows an easy interpretation. But the trends that we have described occur also for an arbitrary stimulus.^[71] The different dependences of g_C , g_s with the voltage shown in **Figure 31** play an important role in the transition of the hysteresis from capacitive to inductive. In **Figure 31a** we show parameters with $g_C > g_s$, that produce standard capacitive hysteresis in **Figure 31b**. On the other hand, in **Figure 31c** there is a crossing of g_C , g_s , and a corresponding change of the type of hysteresis in **Figure 31d**, with

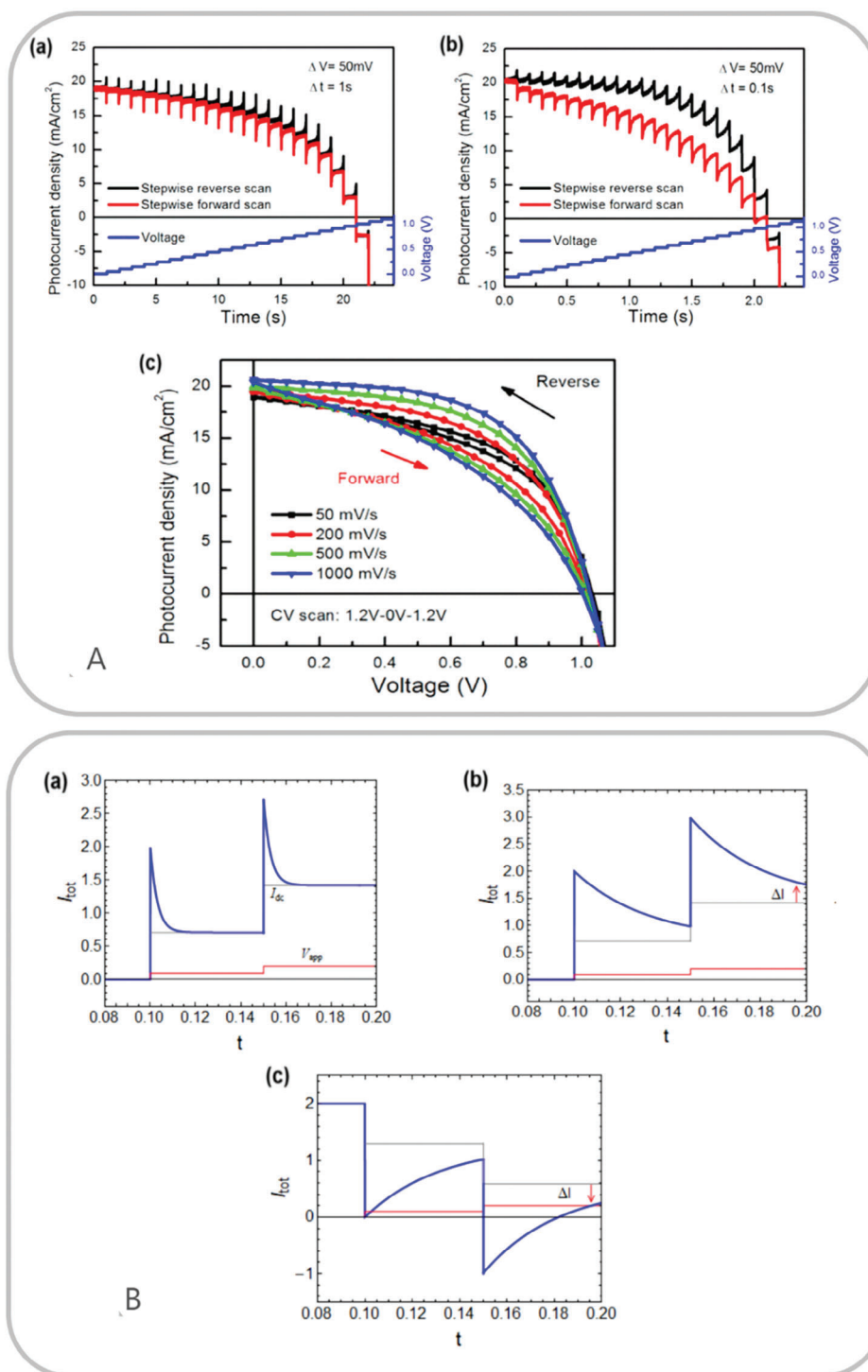


Figure 29. A. Time-dependent photocurrent response of planar perovskite solar cell on compact TiO₂ with 500 nm CH₃NH₃PbI₃ film as the light-absorber layer and 150 nm Spiro-OMeTAD as the hole transport layer under reverse and forward stepwise scans with a) 1 s step time and b) 0.1 s step time. c) Current–voltage response with different scan rates. Reproduced with permission^[17] Copyright 2015, American Chemical Society. B. Current response of the linear model to two consecutive voltage steps, from time t_0 , of duration Δt , first with amplitude $\Delta V = 0.1$ and the second $\Delta V = 0.2$. The common parameters are $R_b = 1$, $R_d = 0.1$, $R_s = 0.05$, $t_0 = 0.1$, $\Delta t = 0.05$, $\tau_k = 0.0005$; The different cases are (a) $C_m = 0.1$, (b) $C_m = 1$, (c) $C_m = 1$, and added photocurrent $I_{ph} = 2$. The red lines are the applied voltage steps and the gray lines indicate the steady state current at the given voltage. The orange arrows indicate the excess current at the end of the cycle, with respect to the steady state value. Reproduced with permission^[84] Copyright 2023, Creative Commons Attribution (CC BY 4.0) license.

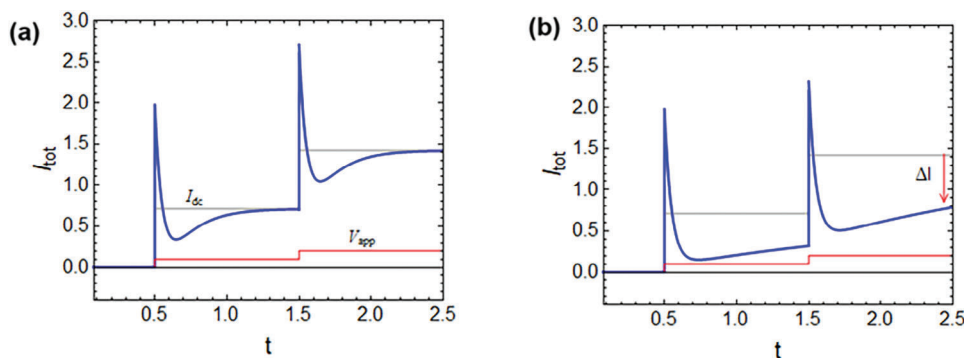


Figure 30. Current response of the linear model to two consecutive voltage steps, from time t_0 , of duration Δt , first with amplitude $\Delta V = 0.1$ and the second $\Delta V = 0.2$. The common parameters are $R_b = 1$, $R_d = 0.1$, $R_s = 0.05$, $t_0 = 0.5$, $\Delta t = 1$, $C_m = 1$. The different cases are (a) (c) $\tau_k = 0.3$; (d) $\tau_k = 3$. The red lines are the applied voltage steps and the gray lines indicate the steady state current at the given voltage. The orange arrows indicate the excess current at the end of the cycle, with respect to the steady state value. Reproduced with permission^[84] Copyright 2023, Creative Commons Attribution (CC BY 4.0) license.

an inductive hysteresis appearing at high voltage, where the g_s dominates. This is the trend observed in Figure 1a.^[72]

Furthermore we can write Equation (97) as:

$$j_{tot} = J_{rec}(u) + C_s(u) \left(\frac{1}{\tau_{rec}(u)} - \frac{1}{\tau_s} \right) S_r \tau_s (1 - e^{-u/S_r \tau_s}) \quad (98)$$

We can see that the crossing point depends on the intrinsic time constants, as in Equation (20). It occurs when

$$\tau_{rec}(u) = \tau_s \quad (99)$$

In the model of Equations (81) and (82) the j_{rec} and C_s functions are coupled by construction^[76,116] and they produce the identity (49), connected with the crossing feature indicated in Equation (32). Alternatively one can start from separate capacitance and current, using the lines E, F in Figure 25. But then experiments indicate that the related time constants C_{ion}/g_{ion} and $g_d L_d$ are the same,^[68,72] and they amount to the time τ_s . This time is called τ_{kin} in the original publications,^[68,72] associated to surface charge reorganization kinetics.

Based on these properties we can establish a general frame-work for the analysis of hysteresis of PSC showing the patterns

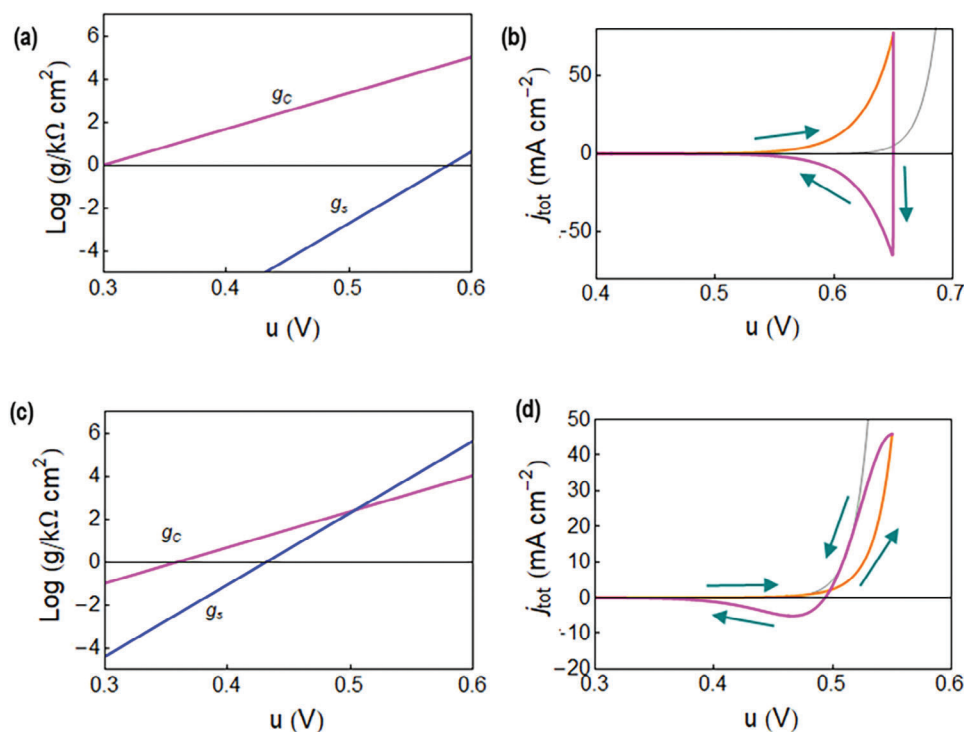


Figure 31. Conductivities and current–voltage curves for stationary (gray) and constant rate scan cycle. Parameters: $k_B T/q = 0.026$ V, $n_r = 1$, $n_s = 1$; $n_r = 0.5$, $\tau_s = 1$ s. a,b) $J_{rec0} = 10^{-21}$ mA cm $^{-2}$, $C_{s0} = 10^{-8}$ F cm $^{-2}$, $V_r = 0.0001$ V s $^{-1}$. c,d) $J_{rec0} = 10^{-16}$ mA cm $^{-2}$, $C_{s0} = 10^{-9}$ F cm $^{-2}$, $V_r = 0.1$ V s $^{-1}$.

Fast transient-based protocol to determine stationary performance of perovskite solar cells with current-voltage hysteresis

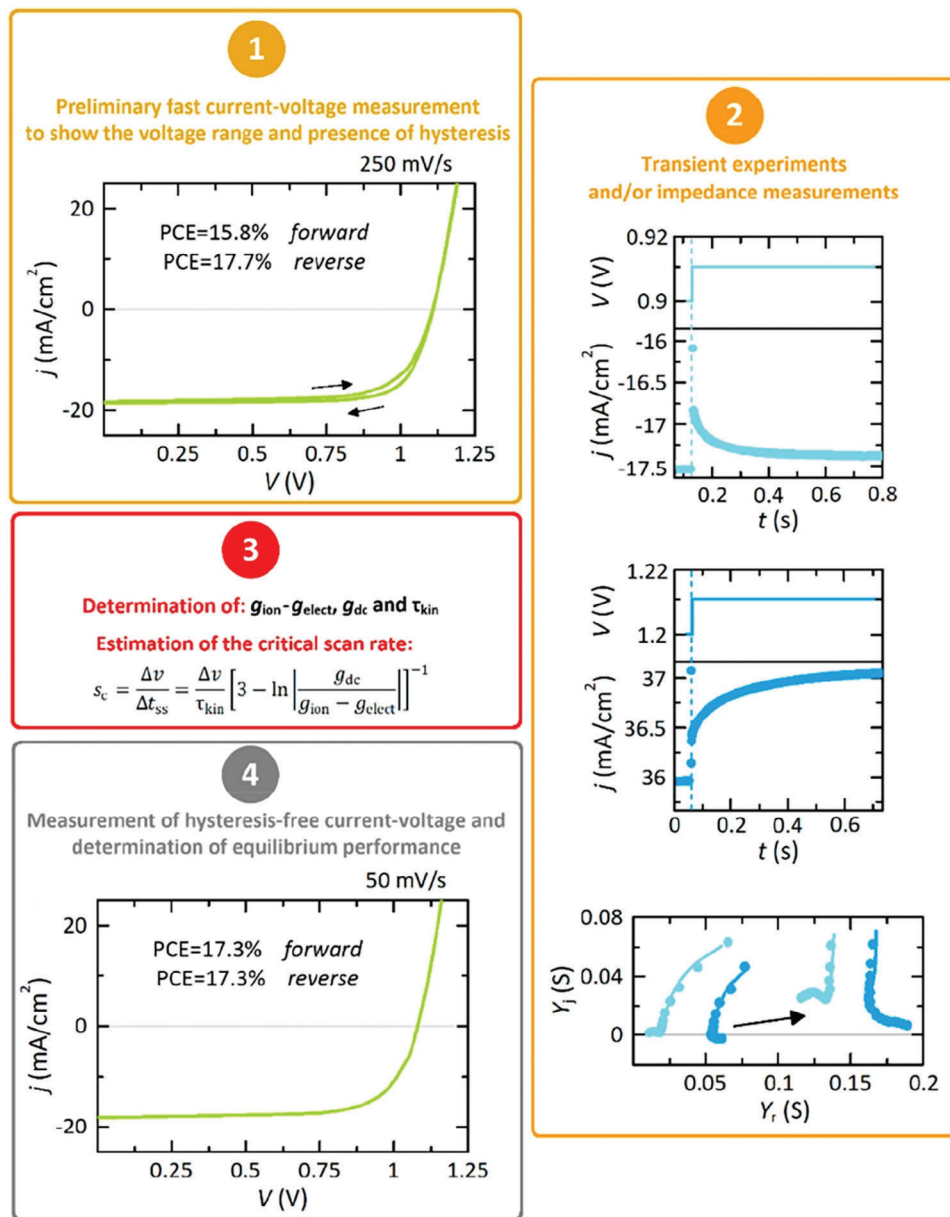


Figure 32. Fast experimental methodology to determine the stationary performance of perovskite solar cells with hysteresis effects. The experimental data correspond to an inverted or p-i-n perovskite device. Reproduced with permission^[72] Copyright 2024, Creative Commons Attribution (CC BY 4.0) license.

of Figure 1. Given a certain voltage step, ΔV , the Balaguera criterion^[72]

$$S_c = \frac{\Delta V}{\Delta t_{ss}} = \frac{\Delta V}{\tau_{kin}} \left[3 - \ln \left| \frac{g_{dc}}{g_c - g_s} \right| \right] \quad (100)$$

provides the shorter time Δt_{ss} in which the current will achieve equilibrium. This leads to the critical scan rate S_c . This is the fastest scan rate at which hysteresis-free curves can be mea-

sured. In Equation (100) g_{dc} is the dc conductance in the model of Figure 18, Equation (33).

The recognition of S_c provides significant opportunities for the fast characterization of PSC as indicated in the methodology of Figure 32.^[72] In addition, this criterion enables to assess the significance of the usual claims of “hysteresis-free” current-voltage curves reported in the literature. In fact, hysteresis curves will be necessarily found for $S_r > S_c$, while apparently hysteresis is suppressed, if measured at $S_r < S_c$. Admitting that

hysteresis effects in PSC are an intrinsic phenomenon, the question is at what kinetic scales it occurs, which depends critically on the relevant relaxation times.^[219] As we have shown this can be rapidly ascertained by impedance or time transient measurements. The reliable reporting of PSC should provide an assessment of the Balaguera number S_c or an equivalent figure.

16. Discussion

Our analysis shows an important connection of both the time domain response and hysteresis of current–voltage curves on the one hand, and the impedance spectroscopy properties, on the other. The important features of the impedance are not only related to describe the different spectra, one by one, at some specific voltages. The main route of analysis is to obtain a global description of how the spectra evolve over a large voltage window, causing the significant features in the time domain response. The neuron-style approach provides an efficient route for an economical model in terms of a few number of parameters that determine the general evolution of the system under many different circumstances. By the identification of the dominant physical features of the transient behavior, represented by states variables and they associated relaxation time, these models can deal with complex experimental situations related to slow recombination effects, or change collection by the applied drift field, under a wide voltage span.

Inspired by the Hodgkin–Huxley models for neuron spiking, the neuron-style models for halide perovskite devices propose a simplified molecular complexity to highlight the dominant dynamical properties. This approach is recommended for analyzing large data sets. To gain detailed insight of a particular device, these methods can be complemented by other approaches which implement particular mechanisms, sometimes using large parameter sets in drift-diffusion approaches.

Of course detailed modelling by drift-diffusion of all the carriers offers enormous opportunities for the realistic modelling of perovskite devices, accounting for effects such as space-charge limitations and multiscale dynamics.^[34,79,103,130,136,169,201,220,221] However, many hysteresis and transient effects in PSC correspond to highly localized effects by surface recombination and charge extraction at the perovskite-transport layer interfaces.^[17,222–225] Resistive switching in halide perovskites can also be strongly localized in nanometer-thick buffer layers, Figure 7.^[137] These effects may be difficult to treat with drift-diffusion models that naturally emphasize specific bulk transport characteristics.

The key aspect for the neuron-style models to achieve their goals is the selection of the right state variables, according to the specific system. We have explored three main alternatives of a memory variable: a surface polarization voltage, a slow current component, and an open-channel conduction probability. There is not a general straightforward way to determine a state variable, that by definition is an internal variable that influences the external input-output variables. The criteria for the selection of state variables are:

1) The knowledge about dominant physical characteristic of the system, i.e., ion displacements, traps,^[82] etc.

2) Satisfying both the current–voltage property and the memory properties, therefore

3) Addressing successfully different static and dynamic measurement techniques.

17. Conclusion

The appearance of variable surface capacitance and inductive properties is substantial to many perovskite devices. In neuron-style models the conduction current associated to the stationary diode behavior is supplemented by history-dependent state variables. This approach provides an excellent analytical tool to deal with systems that combine capacitive and inductive response. With just a few variables, the Hodgkin-Huxley models of neurobiology are able to cope with the intricate dynamical diversity in biological neuron systems of an extraordinary chemical and morphological complexity. Similarly, the neuron-style models applied to perovskite devices are able to identify a few critical parameters such as the dominant kinetic times, that facilitate an excellent account of convolute hysteresis and spiking properties in the time domain response.

According to my understanding of PSCs, they will never be hysteresis-free, if measured at relatively fast scan rates. The question is, whether the underlying hysteresis is significant for the required applications. The time and frequency domain tools that we have summarized, combined with neuron-style models for the interpretation, become important methods to answer such questions.

Acknowledgements

This work was funded by the European Research Council (ERC) via Horizon Europe Advanced Grant, grant agreement no. 101097688 (“Per-oSpiker”). The author is grateful for discussions with Agustín Bou, Enrique H. Balaguera, Antonio Guerrero, and Cedric Gonzales.

Conflict of Interest

The author declares no conflict of interest.

Data Availability Statement

The data presented here can be accessed at <https://doi.org/10.5281/zenodo.10972533> (Zenodo) under the license CC-BY-4.0 (Creative Commons Attribution-ShareAlike 4.0 International).

Keywords

halide perovskites, hysteresis, impedance spectroscopy, memristors, solar cells

Received: January 27, 2024

Revised: April 16, 2024

Published online:

[1] H. Min, D. Y. Lee, J. Kim, G. Kim, K. S. Lee, J. Kim, M. J. Paik, Y. K. Kim, K. S. Kim, M. G. Kim, T. J. Shin, *Nature* **2021**, 598, 444.

- [2] Y. Zhao, F. Ma, Z. Qu, S. Yu, T. Shen, H.-X. Deng, X. Chu, X. Peng, Y. Yuan, X. Zhang, J. You, *Science* **2022**, 377, 531.
- [3] R. S. Sanchez, V. Gonzalez-Pedro, J.-W. Lee, N.-G. Park, Y. S. Kang, I. Mora-Sero, J. Bisquert, *J. Phys. Chem. Lett.* **2014**, 5, 2357.
- [4] E. J. Juarez-Perez, R. S. Sanchez, L. Badia, G. Garcia-Belmonte, V. Gonzalez-Pedro, Y. S. Kang, I. Mora-Sero, J. Bisquert, *J. Phys. Chem. Lett.* **2014**, 5, 2390.
- [5] H.-S. Kim, I. Mora-Sero, V. Gonzalez-Pedro, F. Fabregat-Santiago, E. J. Juarez-Perez, N.-G. Park, J. Bisquert, *Nat. Commun.* **2013**, 4, 2242.
- [6] L. Bertoluzzi, R. S. Sanchez, L. Liu, J.-W. Lee, E. Mas-Marza, H. Han, N.-G. Park, I. Mora-Sero, J. Bisquert, *Energy Environ. Sci.* **2015**, 8, 910.
- [7] R. Gottesman, P. Lopez-Varo, L. Gouda, J. A. Jimenez-Tejada, J. Hu, S. Tirosh, A. Zaban, J. Bisquert, *Chem* **2016**, 7, 776.
- [8] R. Gottesman, E. Haltzi, L. Gouda, S. Tirosh, Y. Bouhadana, A. Zaban, E. Mosconi, F. De Angelis, *J. Phys. Chem. Lett.* **2014**, 5, 2662.
- [9] L. Gouda, R. Gottesman, A. Ginsburg, D. A. Keller, E. Haltzi, J. Hu, S. Tirosh, A. Y. Anderson, A. Zaban, P. P. Boix, *J. Phys. Chem. Lett.* **2015**, 6, 4640.
- [10] A. Baumann, K. Tvingstedt, M. C. Heiber, S. Vath, C. Mombona, H. J. Bolink, V. Dyakonov, *APL Materials* **2014**, 2, 081501.
- [11] H. J. Snaith, A. Abate, J. M. Ball, G. E. Eperon, T. Leijtens, N. K. Noel, S. D. Stranks, J. T.-W. Wang, K. Wojciechowski, W. Zhang, *J. Phys. Chem. Lett.* **2014**, 5, 1511.
- [12] E. L. Unger, E. T. Hoke, C. D. Bailie, W. H. Nguyen, A. R. Bowring, T. Heumüller, M. G. Christoforo, M. D. McGehee, *Energy Environ. Sci.* **2014**, 7, 3690.
- [13] H.-S. Kim, N.-G. Park, *J. Phys. Chem. Lett.* **2014**, 5, 2927.
- [14] S. van Reenen, M. Kemerink, H. J. Snaith, *J. Phys. Chem. Lett.* **2015**, 6, 3808.
- [15] H.-S. Kim, I.-H. Jang, N. Ahn, M. Choi, A. Guerrero, J. Bisquert, N.-G. Park, *J. Phys. Chem. Lett.* **2015**, 6, 4633.
- [16] O. Almora, C. Aranda, I. Zarazua, A. Guerrero, G. Garcia-Belmonte, *ACS Energy Lett* **2016**, 1, 209.
- [17] B. Chen, M. Yang, X. Zheng, C. Wu, W. Li, Y. Yan, J. Bisquert, G. Garcia-Belmonte, K. Zhu, S. Priya, *J. Phys. Chem. Lett.* **2015**, 6, 4693.
- [18] Y. G. Rong, Y. Hu, S. Ravishankar, H. W. Liu, X. M. Hou, Y. S. Sheng, A. J. Mei, Q. F. Wang, D. Y. Li, M. Xu, J. Bisquert, H. W. Han, *Energy Environ. Sci.* **2017**, 10, 2383.
- [19] N. Pellet, F. Giordano, M. Ibrahim Dar, G. Gregori, S. M. Zakeeruddin, J. Maier, M. Grätzel, *Prog. Photov.: Res. Appl.* **2017**, 25, 942.
- [20] F. Wu, R. Pathak, Q. Qiao, *Catalysis Today* **2021**, 374, 86.
- [21] K. Sakhatskyi, R. A. John, A. Guerrero, S. Tsarev, S. Sabisch, T. Das, G. J. Matt, S. Yakunin, I. Cherniukh, M. Kotyrba, Y. Berezovska, M. I. Bodnarchuk, S. Chakraborty, J. Bisquert, M. V. Kovalenko, *ACS Energy Lett* **2022**, 7, 3401.
- [22] A. Senocrate, J. Maier, *J. Am. Chem. Soc.* **2019**, 141, 8382.
- [23] T.-Y. Yang, G. Gregori, N. Pellet, M. Grätzel, J. Maier, *Angew. Chem. Int. Ed.* **2015**, 54, 7905.
- [24] A. Pockett, M. J. Carnie, *ACS Energy Lett* **2017**, 2, 1683.
- [25] D. A. Jacobs, Y. Wu, H. Shen, C. Barugkin, F. J. Beck, T. P. White, K. Weber, K. R. Catchpole, *Phys. Chem. Chem. Phys.* **2017**, 19, 3094.
- [26] A. Guerrero, G. Garcia-Belmonte, I. Mora-Sero, J. Bisquert, Y. S. Kang, T. J. Jacobsson, J.-P. Correa-Baena, A. Hagfeldt, *J. Phys. Chem. C* **2016**, 120, 8023.
- [27] A. Dualeh, T. Moehl, N. Tétreault, J. Teuscher, P. Gao, M. K. Nazeeruddin, M. Grätzel, *ACS Nano* **2014**, 8, 362.
- [28] A. O. Alvarez, R. Arcas, C. A. Aranda, L. Bethencourt, E. Mas-Marzá, M. Saliba, F. Fabregat-Santiago, *J. Phys. Chem. Lett.* **2020**, 11, 8417.
- [29] F. Fabregat-Santiago, M. Kulbak, A. Zohar, M. Vallés-Pelarda, G. Hodes, D. Cahen, I. Mora-Seró, *ACS Energy Lett* **2017**, 2, 2007.
- [30] M. T. Khan, P. Huang, A. Almohammed, S. Kazim, S. Ahmad, *iScience* **2021**, 24, 102024.
- [31] A. Bou, A. Pockett, D. Raptis, T. Watson, M. J. Carnie, J. Bisquert, *J. Phys. Chem. Lett.* **2020**, 11, 8654.
- [32] A. Pockett, D. Raptis, S. M. P. Meroni, J. Baker, T. Watson, M. Carnie, *J. Phys. Chem. C* **2019**, 123, 11414.
- [33] A. Pockett, G. E. Eperon, N. Sakai, H. J. Snaith, L. M. Peter, P. J. M. Cameron, *Phys. Chem. Chem. Phys.* **2017**, 19, 5959.
- [34] R. A. Belisle, W. H. Nguyen, A. R. Bowring, P. Calado, X. Li, S. J. C. Irvine, M. D. McGehee, P. R. F. Barnes, B. C. O'Regan, *Energy Environ. Sci.* **2017**, 10, 192.
- [35] E. Hernández-Balaguera, J. Bisquert, *ACS Energy Lett* **2022**, 7, 2602.
- [36] J. A. Christians, J. S. Manser, P. V. Kamat, *J. Phys. Chem. Lett.* **2015**, 6, 852.
- [37] L. Rakocevic, F. Ernst, N. T. Yimga, S. Vashishtha, T. Aernouts, T. Heumueller, C. J. Brabec, R. Gehlhaar, J. Poortmans, *Solar RRL* **2019**, 3, 1800287.
- [38] H. Köbler, S. Neubert, M. Jankovec, B. Glazar, M. Haase, C. Hilbert, M. Topič, B. Rech, A. Abate, *Energy Technol.* **2022**, 10, 2200234.
- [39] D. V. Christensen, R. Dittmann, B. Linares-Barranco, A. Sebastian, M. Le Gallo, *Neuromorphic Comput. Eng.* **2022**, 2, 022501.
- [40] J. J. Yang, D. B. Strukov, D. R. Stewart, *Nat. Nanotechnol.* **2013**, 8, 13.
- [41] Y. Zhang, Z. Wang, J. Zhu, Y. Yang, M. Rao, W. Song, Y. Zhuo, X. Zhang, M. Cui, L. Shen, R. Huang, J. J. Yang, *Appl. Phys. Rev.* **2020**, 7, 011308.
- [42] J. Zhu, T. Zhang, Y. Yang, R. Huang, *Appl. Phys. Rev.* **2020**, 7, 011312.
- [43] K. Beom, Z. Fan, D. Li, N. Newman, *Mater. Today Phys.* **2022**, 24, 100667.
- [44] A. Mehonic, A. J. Kenyon, *Nature* **2022**, 604, 255.
- [45] G. Indiveri, *Neuromorphic Comput. Eng.* **2021**, 1, 010401.
- [46] W. Wang, E. Covi, A. Milozzi, M. Farronato, S. Ricci, C. Sbandati, G. Pedretti, D. Ielmini, *Adv. Intell. Syst.* **2021**, 3, 2000224.
- [47] *Advances in Neuromorphic Memristor Science and Applications*, (Eds: R. Kozma, R. E. Pino, G. E. Paziienza), Springer, New York **2012**.
- [48] Y. V. Pershin, M. Di Ventra, *Adv. Phys.* **2011**, 60, 145.
- [49] M.-K. Song, J.-H. Kang, X. Zhang, W. Ji, A. Ascoli, I. Messaris, A. S. Demirkol, B. Dong, S. Aggarwal, W. Wan, S.-M. Hong, S. G. Cardwell, I. Boybat, J.-S. Seo, J.-S. Lee, M. Lanza, H. Yeon, M. Onen, J. Li, B. Yildiz, J. A. del Alamo, S. Kim, S. Choi, G. Milano, C. Ricciardi, L. Alf, Y. Chai, Z. Wang, H. Bhaskaran, M. C. Hersam, et al., *ACS Nano* **2023**, 17, 11994.
- [50] S. Kumar, X. Wang, J. P. Strachan, Y. Yang, W. D. Lu, *Nat. Rev. Mater.* **2022**, 7, 575.
- [51] R. Waser, M. Aono, *Nat. Mater.* **2007**, 6, 833.
- [52] L. Chua, *Appl. Phys. A* **2011**, 102, 765.
- [53] B. Linares-Barranco, T. Serrano-Gotarredona, *Nat. Preced.* **2009**, <https://doi.org/10.1038/npre.2009.3010.1031>.
- [54] S. H. Jo, T. Chang, I. Ebong, B. B. Bhadviya, P. Mazumder, W. Lu, *Nano Lett.* **2010**, 10, 1297.
- [55] M. Prezioso, M. R. Mahmoodi, F. M. Bayat, H. Nili, H. Kim, A. Vincent, D. B. Strukov, *Nat. Commun.* **2018**, 9, 5311.
- [56] C. Wang, Z. Si, X. Jiang, A. Malik, Y. Pan, S. Stathopoulos, A. Serb, S. Wang, T. Prodromakis, C. Papavassiliou, *IEEE J. Emerging Selected Topics Circuits Systems* **2022**, 12, 723.
- [57] W. Xu, H. Cho, Y.-H. Kim, Y.-T. Kim, C. Wolf, C.-G. Park, T.-W. Lee, *Adv. Mater.* **2016**, 28, 5916.
- [58] Z. Xiao, J. Huang, *Adv. Electron. Mater.* **2016**, 2, 1600100.
- [59] J. Choi, J. S. Han, K. Hong, S. Y. Kim, H. W. Jang, *Adv. Mater.* **2018**, 30, 1704002.
- [60] R. A. John, N. Yantara, S. E. Ng, M. I. B. Patdillah, M. R. Kulkarni, N. F. Jamaludin, J. Basu, Ankit, S. G. Mhaisalkar, A. Basu, N. Mathews, *Adv. Mater.* **2021**, 33, 2007851.
- [61] J.-Q. Yang, R. Wang, Z.-P. Wang, Q.-Y. Ma, J.-Y. Mao, Y. Ren, X. Yang, Y. Zhou, S.-T. Han, *Nano Energy* **2020**, 74, 104828.

- [62] R. A. John, Y. Demirağ, Y. Shynkarenko, Y. Berezovska, N. Ohannessian, M. Payvand, P. Zeng, M. I. Bodnarchuk, F. Krumeich, G. Kara, I. Shorubalko, M. V. Nair, G. A. Cooke, T. Lippert, G. Indiveri, M. V. Kovalenko, *Nat. Commun.* **2022**, *13*, 2074.
- [63] R. A. John, A. Milozzi, S. Tsarev, R. Brönnimann, S. C. Boehme, E. Wu, I. Shorubalko, M. V. Kovalenko, D. Ielmini, *Sci. Adv.* **2022**, *8*, eade0072.
- [64] J. Zhang, S. Dai, Y. Zhao, J. Zhang, J. Huang, *Adv. Intell. Syst.* **2020**, *2*, 1900136.
- [65] I. Raifuku, Y.-P. Chao, H.-H. Chen, C.-F. Lin, P.-E. Lin, L.-C. Shih, K.-T. Chen, J.-Y. Chen, J.-S. Chen, P. Chen, *EcoMat* **2021**, *3*, e12142.
- [66] Y. Wang, Z. Lv, J. Chen, Z. Wang, Y. Zhou, L. Zhou, X. Chen, S.-T. Han, *Adv. Mater.* **2018**, *30*, 1802883.
- [67] J. Bisquert, *Chem. Phys. Rev.* **2023**, *4*, 031313.
- [68] C. Gonzales, A. Guerrero, J. Bisquert, *J. Phys. Chem. C* **2022**, *126*, 13560.
- [69] J. Bisquert, A. C. I. Guerrero, *J. Am. Chem. Soc.* **2022**, *144*, 5996.
- [70] J. Bisquert, *Appl. Phys. Rev.* **2022**, *9*, 011318.
- [71] J. Bisquert, A. Guerrero, C. Gonzales, *ACS Phys. Chem Au* **2021**, *1*, 25.
- [72] E. H. Balaguera, J. Bisquert, *ACS Energy Lett.* **2024**, *9*, 478.
- [73] E. Hernández-Balaguera, L. Munoz-Diaz, A. Bou, B. Romero, B. Ilyassov, A. Guerrero, J. Bisquert, *Neuromorphic Comput. Eng.* **2023**, *3*, 024005.
- [74] J. Bisquert, A. Bou, A. Guerrero, E. Hernández-Balaguera, *APL Machine Learning* **2023**, *1*, 036101.
- [75] N. Filipoiu, A. T. Preda, D.-V. Anghel, R. Patru, R. E. Brophy, M. Kateb, C. Besleaga, A. G. Tomulescu, I. Pintilie, A. Manolescu, G. A. Nemnes, *Phys. Rev. Appl.* **2022**, *18*, 064087.
- [76] J. Bisquert, *J. Phys. Chem. Lett.* **2023**, *14*, 1014.
- [77] J. Bisquert, C. Gonzales, A. Guerrero, *J. Phys. Chem. C* **2023**, *127*, 21338.
- [78] M. Berruet, J. C. Pérez-Martínez, B. Romero, C. Gonzales, A. M. Al-Mayouf, A. Guerrero, J. Bisquert, *ACS Energy Lett.* **2022**, *7*, 1214.
- [79] D. Moia, I. Gelmetti, P. Calado, W. Fisher, M. Stringer, O. Game, Y. Hu, P. Docampo, D. Lidzey, E. Palomares, J. Nelson, P. R. F. Barnes, *Energy Environ. Sci.* **2019**, *12*, 1296.
- [80] J. Bisquert, *Phys. Rev. Appl.* **2023**, *20*, 044022.
- [81] S. Yudco, J. Bisquert, L. Etgar, *J. Phys. Chem. Lett.* **2023**, *14*, 11610.
- [82] V. Lopez-Richard, R. S. Wengenroth Silva, O. Lipan, F. Hartmann, *J. Appl. Phys.* **2023**, *133*, 134901.
- [83] G. A. Nemnes, C. Besleaga, A. G. Tomulescu, I. Pintilie, L. Pintilie, K. Torfason, A. Manolescu, *Sol. En. Mater. Sol. Cell* **2017**, *159*, 197.
- [84] J. Bisquert, *PRX Energy* **2023**, *3*, 011001.
- [85] J. Bisquert, *J. Phys. Chem. Lett.* **2023**, *14*, 10951.
- [86] P. Ramirez, A. Bou, J. Cervera, J. Bisquert, *Res. Square* **2023**, <https://doi.org/10.21203/rs.21203.rs-3399146/v3399141>.
- [87] A. Guerrero, J. Bisquert, G. Garcia-Belmonte, *Chemical Reviews* **2021**, *121*, 14430.
- [88] E. Ghahremanirad, O. Almora, S. Suresh, A. A. Drew, T. H. Chowdhury, A. R. Uhl, *Adv. Energy Mater.* **2023**, *13*, 2204370.
- [89] E. von Hauff, D. Klotz, *J. Mat. Chem. C* **2022**, *10*, 742.
- [90] M. A. Afroz, C. A. Aranda, N. K. Tailor, Yukta, P. Yadav, M. M. Tavakoli, M. Saliba, S. Satapathi, *ACS Energy Lett* **2021**, *6*, 3275.
- [91] S. Vinayak Pandey, D. Prochowicz, A. Mahapatra, S. Pandiaraj, A. Alohayb, S. Akin, P. Yadav, *Journal of Energy Chemistry* **2024**, *94*, 393.
- [92] Z. S. Wang, F. Ebadi, B. Carlsen, W. C. H. Choy, W. Tress, *Small Methods* **2020**, *4*, 2000290.
- [93] A. Pockett, M. Spence, S. K. Thomas, D. Raptis, T. Watson, M. J. Carnie, *Solar RRL* **2021**, *5*, 2100159.
- [94] F. Ebadi, N. Taghavinia, R. Mohammadpour, A. Hagfeldt, W. Tress, *Nat. Commun.* **2019**, *10*, 1574.
- [95] S. E. J. O'Kane, G. Richardson, A. Pockett, R. G. Niemann, J. M. Cave, N. Sakai, G. E. Eperon, H. J. Snaith, J. M. Foster, P. J. Cameron, A. B. Walker, *J. Mat. Chem. C* **2017**, *5*, 452.
- [96] P. Andričević, M. Kollár, X. Mettan, B. Náfrádi, A. Sienkiewicz, D. Fejes, K. Hernádi, L. Forró, E. Horváth, *J. Phys. Chem. C* **2017**, *121*, 13549.
- [97] K. Mantulnikovs, A. Glushkova, M. Kollár, L. Forró, E. Horváth, A. Sienkiewicz, *ACS Applied Electronic Materials* **2019**, *1*, 2007.
- [98] P. Wangyang, C. Gong, G. Rao, K. Hu, X. Wang, C. Yan, L. Dai, C. Wu, J. Xiong, *Adv. Opt. Mater.* **2018**, *6*, 1701302.
- [99] A. Mahapatra, V. Anilkumar, J. Nawrocki, S. V. Pandey, R. D. Chavan, P. Yadav, D. Prochowicz, *Adv. Electron. Mater.* **2023**, *9*, 2300226.
- [100] A. Mahapatra, V. Anilkumar, R. D. Chavan, P. Yadav, D. Prochowicz, *ACS Photonics* **2023**, *10*, 1424.
- [101] A. Zaban, M. Greenshtein, J. Bisquert, *ChemPhysChem* **2003**, *4*, 859.
- [102] D. Kiermasch, A. Baumann, M. Fischer, V. Dyakonov, K. Tvingstedt, *Energy Environ. Sci.* **2018**, *11*, 629.
- [103] S. Ravishankar, L. Kruppa, S. Jenatsch, G. Yan, Y. Wang, *Energy Environ. Sci.* **2024**, *17*, 1229.
- [104] M. T. Neukom, A. Schiller, S. Züfle, E. Knapp, J. Ávila, D. Pérez-del-Rey, C. Dreessen, K. P. S. Zanoni, M. Sessolo, H. J. Bolink, B. Ruhstaller, *ACS Appl. Mat. Int.* **2019**, *11*, 23320.
- [105] E. Zimmermann, P. Ehrenreich, T. Pfadler, J. A. Dorman, J. Weickert, L. Schmidt-Mende, *Nature Photonics* **2014**, *8*, 669.
- [106] Y. Wang, X. Liu, Z. Zhou, P. Ru, H. Chen, X. Yang, L. Han, *Adv. Mater.* **2019**, *31*, 1803231.
- [107] F. Wu, R. Pathak, Q. Qiao, *Catal. Today* **2021**, *374*, 86.
- [108] M. T. Neukom, S. Züfle, E. Knapp, M. Makha, R. Hany, B. Ruhstaller, *Sol. En. Mater. Sol. Cell* **2017**, *169*, 159.
- [109] R. Yekani, H.-c. Chiu, D. Strandell, Z. Wang, S. Bessette, R. Gauvin, P. Kambhampati, G. P. Demopoulos, *Nanoscale* **2023**, *15*, 2152.
- [110] O. Almora, I. Zarazua, E. Mas-Marza, I. Mora-Sero, J. Bisquert, G. Garcia-Belmonte, *J. Phys. Chem. Lett.* **2015**, *6*, 1645.
- [111] G. Garcia-Belmonte, J. Bisquert, *ACS Energy Lett* **2016**, *1*, 683.
- [112] D. A. Jacobs, H. Shen, F. Pfeffer, J. Peng, T. P. White, F. J. Beck, K. R. Catchpole, *J. Appl. Phys.* **2018**, *124*, 225702.
- [113] M. Taukeer Khan, F. Khan, A. Al-Ahmed, S. Ahmad, F. Al-Sulaiman, *The Chemical Record* **2022**, 202100330.
- [114] E. J. Juarez-Perez, C. Mombiona, R. Casas, M. Haro, *Cell Reports Physical Science* **2024**, *5*.
- [115] S. Ravishankar, O. Almora, C. Echeverría-Arrondo, E. Ghahremanirad, C. Aranda, A. Guerrero, F. Fabregat-Santiago, A. Zaban, G. Garcia-Belmonte, J. Bisquert, *J. Phys. Chem. Lett.* **2017**, *9*, 915.
- [116] E. Ghahremanirad, A. Bou, S. Olyaei, J. Bisquert, *J. Phys. Chem. Lett.* **2017**, *8*, 1402.
- [117] P. Würfel *Physics of Solar Cells. From Principles to New Concepts. Second edition*, Wiley, Weinheim, **2009**.
- [118] J. Nelson *The Physics of Solar Cells*, Imperial College Press, London, **2003**.
- [119] P. K. Nayak, J. Bisquert, D. Cahen, *Adv. Mater.* **2011**, *23*, 2870.
- [120] A. Hagfeldt, M. Grätzel, *Acc. Chem. Res.* **2000**, *33*, 269.
- [121] S. Södergren, A. Hagfeldt, J. Olsson, S. E. Lindquist, *J. Phys. Chem.* **1994**, *98*, 5552.
- [122] J. Bisquert, *Phys. Chem. Chem. Phys.* **2003**, *5*, 5360.
- [123] J. Warby, S. Shah, J. Thiesbrummel, E. Gutierrez-Partida, H. Lai, B. Alebachew, M. Grischek, F. Yang, F. Lang, S. Albrecht, F. Fu, D. Neher, M. Stollerfoht, *Adv. Energy Mater.* **2023**, *13*, 2303135.
- [124] X. Liu, D. Luo, Z.-H. Lu, J. S. Yun, M. Saliba, S. I. Seok, W. Zhang, *Nature Reviews Chemistry* **2023**, *7*, 462.
- [125] L. Schmidt-Mende, V. Dyakonov, S. Olthof, F. Ünlü, K. M. T. Lê, S. Mathur, A. D. Karabanov, D. C. Lupascu, L. M. Herz, A. Hinderhofer, *APL Materials* **2021**, *9*, 109202.
- [126] Y. Zhou, L. M. Herz, A. K. Y. Jen, M. Saliba, *Nat. Energy* **2022**, *7*, 794.

- [127] J. Bisquert *The Physics of Solar Energy Conversion*, CRC Press, Boca Raton, **2020**.
- [128] J.-P. Correa-Baena, S.-H. Turren-Cruz, W. Tress, A. Hagfeldt, C. Aranda, L. Shooshtari, J. Bisquert, A. Guerrero, *ACS Energy Lett* **2017**, 681.
- [129] J. Chen, N.-G. Park, *Adv. Mater.* **2019**, 31, 1803019.
- [130] C. M. Wolff, P. Caprioglio, M. Stolterfoht, D. Neher, *Adv. Mater.* **2019**, 31, 1902762.
- [131] O. Almora, K. T. Cho, S. Aghazada, I. Zimmermann, G. J. Matt, C. J. Brabec, M. K. Nazeeruddin, G. Garcia-Belmonte, *Nano Energy* **2018**, 48, 63.
- [132] C. M. Wolff, S. A. Bouelle, L. Q. Phuong, J. Kurpiers, S. Feldmann, P. Caprioglio, J. A. Marquez, J. Wolansky, T. Unold, M. Stolterfoht, S. Shoaee, F. Deschler, *Adv. Energy Mater.* **2021**, 11, 2101823.
- [133] P. Caprioglio, C. M. Wolff, O. J. Sandberg, A. Armin, B. Rech, S. Albrecht, D. Neher, M. Stolterfoht, *Adv. Energy Mater.* **2020**, 10, 2000502.
- [134] E. Aydin, J. Liu, E. Ugur, R. Azmi, G. T. Harrison, Y. Hou, B. Chen, S. Zhumagali, M. De Bastiani, M. Wang, W. Raja, T. G. Allen, A. u. Rehman, A. S. Subbiah, M. Babics, A. Babayigit, F. H. Isikgor, K. Wang, E. Van Kerschaver, L. Tsetseris, E. H. Sargent, F. Laquai, S. De Wolf, *Energy Environ. Sci.* **2021**, 14, 4377.
- [135] P. Calado, A. M. Telford, D. Bryant, X. Li, J. Nelson, B. C. O'Regan, P. R. F. Barnes, *Nat. Commun.* **2016**, 7, 13831.
- [136] G. A. Nemnes, C. Besleaga, V. Stancu, D. E. Dogaru, L. N. Leonat, L. Pintilie, K. Torfason, M. Ilkov, A. Manolescu, *J. Phys. Chem. C* **2017**, 121, 11207.
- [137] C. Gonzales, A. Guerrero, *J. Phys. Chem. Lett.* **2023**, 14, 1395.
- [138] H.-L. Park, Y. Lee, N. Kim, D.-G. Seo, G.-T. Go, T.-W. Lee, *Adv. Mater.* **2020**, 32, 1903558.
- [139] M. Loizos, K. Rogdakis, E. Kymakis, *Discover Mater.* **2022**, 2, 11.
- [140] J. B. Roldán, E. Miranda, D. Maldonado, A. N. Mikhaylov, N. V. Agudov, A. A. Dubkov, M. N. Koryazhkina, M. B. González, M. A. Villena, S. Poblador, M. Saludes-Tapia, R. Picos, F. Jiménez-Molinos, S. G. Stavriniades, E. Salvador, F. J. Alonso, F. Campabadal, B. Spagnolo, M. Lanza, L. O. Chua, *Adv. Intell. Syst.* **2023**, 5, 2200338.
- [141] M. Lanza, A. Sebastian, W. D. Lu, M. Le Gallo, M.-F. Chang, D. Akinwande, F. M. Puglisi, H. N. Alshareef, M. Liu, J. B. Roldan, *Science* **2022**, 376, eabj9979.
- [142] A. Chen, W. Zhang, L. R. Dedon, D. Chen, F. Khatkhatay, J. L. MacManus-Driscoll, H. Wang, D. Yarotski, J. Chen, X. Gao, L. W. Martin, A. Roelofs, *Adv. Func. Mater.* **2020**, 30, 2000664.
- [143] J. C. Pérez-Martínez, M. Berruet, C. Gonzales, S. Salehpour, A. Bahari, B. Arredondo, A. Guerrero, *Adv. Func. Mater.* **2023**, 33, 2305211.
- [144] K. Rogdakis, K. Chatzimanolis, G. Psaltakis, N. Tzoganakis, D. Tsikritzis, T. D. Anthopoulos, E. Kymakis, *Adv. Electron. Mater.* **2023**, 9, 2300424.
- [145] H. R. Wilson *Spikes, Decisions, and Actions: The Dynamical Foundations of Neuroscience*, Oxford University Press, Oxford **1999**.
- [146] T. F. Weiss *Cellular Biophysics, vol. 2. Electrical Properties*, MIT, Cambridge, MA **1996**.
- [147] P. C. Harikesh, C.-Y. Yang, D. Tu, J. Y. Gerasimov, A. M. Dar, A. Armada-Moreira, M. Massetti, R. Kroon, D. Bliman, R. Olsson, E. Stavrinidou, M. Berggren, S. Fabiano, *Nat. Commun.* **2022**, 13, 901.
- [148] N. Ofer, O. Shefi, G. Yaari, *Sci. Rep.* **2017**, 7, 8877.
- [149] A. L. Hodgkin, A. F. Huxley, *J. Physiol.* **1952**, 117, 500.
- [150] M. Häusser, *Nat. Neurosci.* **2000**, 3, 1165.
- [151] A. J. Hopper, H. Beswick-Jones, A. M. Brown, *Adv. Physiol. Edu.* **2022**, 46, 580.
- [152] W. Gerstner, W. M. Kistler, R. Naud, L. Paninski *Neuronal Dynamics. From Single Neurons to Networks and Models of Cognition*, Cambridge University Press, Cambridge, England **2014**.
- [153] E. M. Izhikevich *Dynamical Systems in Neuroscience*, MIT Press, Cambridge, MA **2007**.
- [154] C. Koch, I. Segev *Methods in Neuronal Modeling, second edition: From Ions to Networks*, MIT Press, Cambridge, MA **2003**.
- [155] *Computational Cell Biology*, (Ed.: C. P. Fall, E. S. Marland, J. M. Wagner, J. J. Tyson), Springer, New York **2002**.
- [156] P. Miller *An Introductory Course in Computational Neuroscience*, MIT Press, Cambridge, MA **2018**.
- [157] M. D. Ventra, Y. V. Pershin, L. O. Chua, *Proc. IEEE* **2009**, 97, 1717.
- [158] T. Prodromakis, C. Toumazou, L. Chua, *Nat. Mater.* **2012**, 11, 478.
- [159] S. Menzel, S. Tappertzhofen, R. Waser, I. Valov, *Phys. Chem. Chem. Phys.* **2013**, 15, 6945.
- [160] D. B. Strukov, G. S. Snider, D. R. Stewart, R. S. Williams, *Nature* **2008**, 453, 80.
- [161] L. O. Chua, K. Sung Mo, *Proc. IEEE* **1976**, 64, 209.
- [162] J. Bisquert, *Chem. Phys. Rev.* **2022**, 3, 041305.
- [163] J. Bisquert, H. Randriamahazaka, G. Garcia-Belmonte, *Electrochimica Acta* **2005**, 51, 627.
- [164] H. Göhr, C.-A. Schiller, *Zeitschrift für Physikalische Chem.* **1986**, 148, 105.
- [165] C. A. Schiller, F. Richter, E. Gülzow, N. Wagner, *Phys. Chem. Chem. Phys.* **2001**, 3, 2113.
- [166] J. Bisquert, A. Guerrero, *J. Phys. Chem. Lett.* **2022**, 13, 3789.
- [167] J. Bisquert, *J. Phys. Chem. Lett.* **2023**, 9027.
- [168] P. C. Harikesh, C.-Y. Yang, H.-Y. Wu, S. Zhang, M. J. Donahue, A. S. Caravaca, J.-D. Huang, P. S. Olofsson, M. Berggren, D. Tu, S. Fabiano, *Nat. Mater.* **2023**, 22, 242.
- [169] W. Tress, J. P. Correa Baena, M. Saliba, A. Abate, M. Graetzel, *Adv. Energy Mater.* **2016**, 6, 1600396.
- [170] I. Mora-Seró, J. Bisquert, F. Fabregat-Santiago, G. Garcia-Belmonte, G. Zoppi, K. Durose, Y. Y. Proskuryakov, I. Oja, A. Belaidi, T. Dittrich, R. Tenza-Zaera, A. Katty, C. Lévy-Clement, V. Barrioz, S. J. C. Irvine, *Nano Lett.* **2006**, 6, 640.
- [171] A. Zohar, N. Kedem, I. Levine, D. Zohar, A. Vilan, D. Ehre, G. Hodes, D. Cahen, *J. Phys. Chem. Lett.* **2016**, 7, 191.
- [172] H. Dhifaoui, N. H. Hemasiri, W. Aloui, A. Bouazizi, S. Kazim, S. Ahmad, *Advanced Materials Interfaces* **2021**, 8, 2101002.
- [173] C. A. Aranda, A. O. Alvarez, V. S. Chivrony, C. Das, M. Rai, M. Saliba, *Joule* **2024**, 8, 241.
- [174] A. Bou, J. Bisquert, *J. Phys. Chem. B* **2021**, 125, 9934.
- [175] I. Fernandez-Guillen, C. A. Aranda, P. F. Betancur, M. Vallés-Pelarda, C. Mombiona, T. S. Ripolles, R. Abargues, P. P. Boix, *Adv. Electron. Mater.* **2024**, 2300475.
- [176] L. Krückemeier, Z. Liu, B. Krogmeier, U. Rau, T. Kirchartz, *Adv. Energy Mater.* **2021**, 11, 2102290.
- [177] J. Bisquert, *J. Phys. Chem. Lett.* **2022**, 13, 7320.
- [178] I. Zarazua, G. Han, P. P. Boix, S. Mhaisalkar, F. Fabregat-Santiago, I. Mora-Seró, J. Bisquert, G. Garcia-Belmonte, *J. Phys. Chem. Lett.* **2016**, 7, 5105.
- [179] T. Kostova, R. Ravindran, M. Schonbek, *Int. J. Bifurcation Chaos* **2004**, 14, 913.
- [180] R. Brette, W. Gerstner, *J. Neurophysiol.* **2005**, 94, 3637.
- [181] H. Deng, X. Yang, D. Dong, B. Li, D. Yang, S. Yuan, K. Qiao, Y.-B. Cheng, J. Tang, H. Song, *Nano Lett.* **2015**, 15, 7963.
- [182] J. Yao, T. Kirchartz, M. S. Vezie, M. A. Faist, W. Gong, He, H. Wu, J. Troughton, T. Watson, D. Bryant, J. Nelson, *Phys. Rev. Appl.* **2015**, 4, 014020.
- [183] G. Xing, N. Mathews, S. Sun, S. S. Lim, Y. M. Lam, M. Gratzel, S. Mhaisalkar, T. C. Sum, *Science* **2013**, 342, 344.
- [184] T. Kirchartz, J. Bisquert, I. Mora-Sero, G. Garcia-Belmonte, *Phys. Chem. Chem. Phys.* **2015**, 17, 4007.
- [185] J.-Y. Huang, Y.-W. Yang, W.-H. Hsu, E.-W. Chang, M.-H. Chen, Y.-R. Wu, *Sci. Rep.* **2022**, 12, 7927.

- [186] R. García-Rodríguez, A. J. Riquelme, M. Cowley, K. Valadez-Villalobos, G. Oskam, L. J. Bennett, M. J. Wolf, L. Contreras-Bernal, P. J. Cameron, A. B. Walker, J. A. Anta, *Energy Technol.* **2022**, *10*, 2200507.
- [187] O. Almora, P. Lopez-Varo, K. T. Cho, S. Aghazada, W. Meng, Y. Hou, C. Echeverría-Arrondo, I. Zimmermann, G. J. Matt, J. A. Jiménez-Tejada, C. J. Brabec, M. K. Nazeeruddin, G. Garcia-Belmonte, *Sol. Energy Mater. Sol. Cell* **2019**, *195*, 291.
- [188] J. Thiesbrummel, S. Shah, E. Gutierrez-Partida, F. Zu, F. Peña-Camargo, S. Zeiske, J. Diekmann, F. Ye, K. P. Peters, K. O. Brinkmann, P. Caprioglio, A. Dasgupta, S. Seo, F. A. Adeleye, J. Warby, Q. Jeangros, F. Lang, S. Zhang, S. Albrecht, T. Riedl, A. Armin, D. Neher, N. Koch, Y. Wu, V. M., Le Corre, H. Snaith, M. Stolterfoht, *Nat. Energy* **2024**.
- [189] R. Wessel, W. B. Kristan Jr, D. Kleinfeld, *J. Neurosci.* **1999**, *19*, 5875.
- [190] J. Cervera, S. Meseguer, S. Mafe, *Sci. Rep.* **2016**, *6*, 35201.
- [191] J. Cervera, J. A. Manzanares, S. Mafe, *J. Phys. Chem. B* **2015**, *119*, 2968.
- [192] C. C. Ceballos, A. C. Roque, R. M. Leão, *Biophys. Rev.* **2017**, *9*, 827.
- [193] B. Hille *Ion Channels of Excitable Membranes*, Sinauer Associates, Sunderland, MA **1992**.
- [194] K. Williams, *Cellular Signal.* **1997**, *9*, 1.
- [195] C. M. Armstrong, *Quarterly Rev. Biophys.* **1974**, *7*, 179.
- [196] F. L. Aguirre, J. Suñé, E. Miranda, *Micromachines* **2022**, *13*, 330.
- [197] E. Miranda, J. Suñé, *IEEE Trans. Nanotechnol.* **2020**, *19*, 837.
- [198] J. Bisquert, E. Miranda, J. B. Roldan, *PhysChemChemPhys* **2024**.
- [199] W. Chen, S. Tappertzshofen, H. J. Barnaby, M. N. Kozicki, *Journal of Electroceramics* **2017**, *39*, 109.
- [200] R. A. John, N. Shah, S. K. Vishwanath, S. E. Ng, B. Febriansyah, M. Jagadeeswararao, C.-H. Chang, A. Basu, N. Mathews, *Nat. Commun.* **2021**, *12*, 3681.
- [201] H. Shen, D. A. Jacobs, Y. Wu, T. Duong, J. Peng, X. Wen, X. Fu, S. K. Karuturi, T. P. White, K. Weber, K. R. Catchpole, *J. Phys. Chem. Lett.* **2017**, *8*, 2672.
- [202] D. Moia, M. Jung, Y.-R. Wang, J. Maier, *Phys. Chem. Chem. Phys.* **2023**, *25*, 13335.
- [203] M. García-Batlle, J. Mayén Guillén, M. Chapran, O. Baussens, J. Zaccaro, J.-M. Verilhac, E. Gros-Daillon, A. Guerrero, O. Almora, G. Garcia-Belmonte, *ACS Energy Lett* **2022**, *7*, 946.
- [204] W. Peng, C. Aranda, O. M. Bakr, G. Garcia-Belmonte, J. Bisquert, A. Guerrero, *ACS Energy Lett* **2018**, *3*, 1477.
- [205] S.-M. Yoo, S. J. Yoon, J. A. Anta, H. J. Lee, P. P. Boix, I. Mora-Seró, *Joule* **2019**, *3*, 2535.
- [206] E. Hernandez-Balaguera, J. Bisquert, *Adv. Func. Mater.* **2023**, *34*, 2308678.
- [207] S. Liu, J. Guan, L. Yin, L. Zhou, J. Huang, Y. Mu, S. Han, X. Pi, G. Liu, P. Gao, S. Zhou, *J. Phys. Chem. Lett.* **2022**, *13*, 10994.
- [208] P. Ramirez, V. Gomez, J. Cervera, S. Mafe, J. Bisquert, *J. Phys. Chem. Lett.* **2023**, *14*, 10930.
- [209] R. S. W. Silva, F. Hartmann, V. Lopez-Richard, *IEEE Trans. Electron Devices* **2022**, *69*, 5351.
- [210] X. Yang, Z. Xiong, Y. Chen, Y. Ren, L. Zhou, H. Li, Y. Zhou, F. Pan, S.-T. Han, *Nano Energy* **2020**, *78*, 105246.
- [211] J. Gong, H. Wei, Y. Ni, S. Zhang, Y. Du, W. Xu, *Mater. Today Phys.* **2021**, *21*, 100540.
- [212] S. Ham, S. Choi, H. Cho, S.-I. Na, G. Wang, *Adv. Func. Mater.* **2019**, *29*, 1806646.
- [213] J. Lao, W. Xu, C. Jiang, N. Zhong, B. Tian, H. Lin, C. Luo, J. Travas-sejdic, H. Peng, C.-G. Duan, *J. Mat. Chem. C* **2021**, *9*, 5706.
- [214] N. Ilyas, D. Li, C. Li, X. Jiang, Y. Jiang, W. Li, *Nanoscale Res. Lett.* **2020**, *15*, 30.
- [215] J. Ding, W. Gao, L. Gao, K. Lu, Y. Liu, J.-L. Sun, Q. Yan, *J. Phys. Chem. Lett.* **2022**, *13*, 7831.
- [216] L. Chen, C. Li, T. Huang, Y. Chen, S. Wen, J. Qi, *Phys. Lett. A* **2013**, *377*, 3260.
- [217] T. Chang, S.-H. Jo, K.-H. Kim, P. Sheridan, S. Gaba, W. Lu, *Appl. Phys. A* **2011**, *102*, 857.
- [218] D. K. Purohit, S. V. Pandey, A. Kalam, S. Akin, S. Satapathi, D. Prochowicz, P. Yadav, *J. Phys. Chem. C* **2023**, *127*, 18185.
- [219] D. Bryant, S. Wheeler, B. C. O'Regan, T. Watson, P. R. F. Barnes, D. Worsley, J. Durrant, *J. Phys. Chem. Lett.* **2015**, *6*, 3190.
- [220] W. Clarke, M. V. Cowley, M. J. Wolf, P. Cameron, A. Walker, G. Richardson, *J. Appl. Phys.* **2023**, *133*, 095001.
- [221] N. Tessler, Y. Vaynzof, *ACS Energy Lett.* **2020**, *5*, 1260.
- [222] C. Das, R. Roy, M. Kedia, M. Kot, W. Zuo, R. Félix, T. Sobol, J. I. Flege, M. Saliba, *ACS Appl. Mat. Int.* **2023**, *15*, 56500.
- [223] J.-P. Correa-Baena, W. Tress, K. Domanski, E. H. Anaraki, S.-H. Turren-Cruz, B. Roose, P. P. Boix, M. Grätzel, M. Saliba, A. Abate, *Energy Environ. Sci.* **2017**, *10*, 1207.
- [224] J.-P. Correa-Baena, A. Abate, M. Saliba, W. Tress, T. Jesper Jacobsson, M. Grätzel, A. Hagfeldt, *Energy Environ. Sci.* **2017**, *10*, 710.
- [225] G. Richardson, S. E. J. O'Kane, R. G. Niemann, T. A. Peltola, J. M. Foster, P. J. Cameron, A. B. Walker, *Energy Environ. Sci.* **2016**, *9*, 1476.



Juan Bisquert has focused his research activity on materials and devices for solar cells and energy storage, summarized in the book *Physics of Solar Energy Conversion* (CRC Press 2020). Recently he addressed the switching perovskite devices such as memristors that find use in memory applications. The main goal of research is to create miniature devices that operate as neurons and synapses for bio-inspired neuromorphic computation related to data sensing and image processing. He has been awarded a ERC Advanced Grant to develop perovskite spiking network for brain-like computational applications.